Not Just a Dot: The Complex UV Morphology and Underlying Properties of Little Red Dots

P. Rinaldi[1,2,21] , N. Bonaventura[1,21] , G. H. Rieke[1] , S. Alberts[1] , K. I. Caputi[2,3] , W. M. Baker[4,5,6] , S. Baum[7] ,
R. Bhatawdekar[8] , A. J. Bunker[9] , S. Carniani[10] , E. Curtis-Lake[11] , F. D'Eugenio[4,12] , E. Egami[1] , Z. Ji[1] ,
B. D. Johnson[13] , K. Hainline[1] , J. M. Helton[1] , X. Lin[1,14] , J. Lyu[1] , Z. Ma[1] , R. Maiolino[4,5,15] ,
P. G. Pérez-González[16] , M. Rieke[1] , B. E. Robertson[17] , I. Shivaei[16] , M. Stone[1] , Y. Sun[1] , S. Tacchella[4,12] ,
H. Übler[18] , C. C. Williams[19] , C. N. A. Willmer[1] , C. Willott[20] , J. Zhang[1] , and Y. Zhu[1]

[1] Steward Observatory, University of Arizona, 933 North Cherry Avenue, Tucson, AZ 85721, USA; prinaldi@arizona.edu
[2] Kapteyn Astronomical Institute, University of Groningen, P.O. Box 800, 9700AV Groningen, The Netherlands
[3] Cosmic Dawn Center (DAWN), Copenhagen, Denmark
[4] Kavli Institute for Cosmology, University of Cambridge, Madingley Road, Cambridge, CB3 OHA, UK
[5] Cavendish Laboratory - Astrophysics Group, University of Cambridge, 19 JJ Thomson Avenue, Cambridge, CB3 OHE, UK
[6] DARK, Niels Bohr Institute, University of Copenhagen, Jagtvej 128, DK-2200 Copenhagen, Denmark
[7] Department of Physics and Astronomy, University of Manitoba, Winnipeg, MB R3T 2N2, Canada
[8] European Space Agency (ESA), European Space Astronomy Centre (ESAC), Camino Bajo del Castillo s/n, 28692 Villanueva de la Cañada, Madrid, Spain
[9] Department of Physics, University of Oxford, Denys Wilkinson Building, Keble Road, Oxford OX13RH, UK
[10] Scuola Normale Superiore, Piazza dei Cavalieri 7, I-56126 Pisa, Italy
[11] Centre for Astrophysics Research, Department of Physics, Astronomy and Mathematics, University of Hertfordshire, Hatfield AL10 9AB, UK
[12] Cavendish Laboratory, University of Cambridge, 19 JJ Thomson Avenue, Cambridge, CB3 0HE, UK
[13] Center for Astrophysics | Harvard & Smithsonian, 60 Garden Street, Cambridge MA 02138, USA
[14] Department of Astronomy, Tsinghua University, Beijing 100084, People's Republic of China
[15] Department of Physics and Astronomy, University College London, Gower Street, London WC1E 6BT, UK
[16] Centro de Astrobiología (CAB), CSIC-INTA, Carretera de Ajalvir Km. 4, 28850 Torrejón de Ardoz, Madrid, Spain
[17] Department of Astronomy and Astrophysics, University of California, Santa Cruz, 1156 High Street, Santa Cruz, CA 95064, USA
[18] Max-Planck-Institut für extraterrestrische Physik (MPE), Gießenbachstraße 1, 85748 Garching, Germany
[19] NSF National Optical-Infrared Astronomy Research Laboratory, 950 North Cherry Avenue, Tucson, AZ 85719, USA
[20] NRC Herzberg, 5071 West Saanich Road, Victoria, BC V9E 2E7, Canada

Abstract

We analyze 99 photometrically selected Little Red Dots (LRDs) at $z \approx$ 4–8 in the GOODS fields, leveraging ultradeep JADES NIRCam short-wavelength (SW) data. Among the 99 selected LRDs, we examine the morphology of 30. The remaining 69 appear predominantly compact, with sizes $\lesssim$400 pc and no extended components even in stacked SW images. However, their unresolved nature may partly reflect current depth limitations, which could prevent the detection of faint diffuse components. Among the 30 morphologically analyzed LRDs, 50% show multiple associated components, while the rest exhibit highly asymmetric structures, despite appearing as single sources. This diversity in rest-frame UV morphologies may point to interactions or strong internal feedback. We find median stellar masses of $\log_{10}(M_\star/M_\odot) = 9.07^{+0.11}_{-0.08}$ for pure stellar models with $A_V \approx 1.16^{+0.11}_{-0.21}$ mag, and $\log_{10}(M_\star/M_\odot) = 9.67^{+0.17}_{-0.27}$ for models including active galactic nuclei (AGNs) with $A_V \approx 2.74^{+0.55}_{-0.71}$ mag, in line with recent studies suggesting higher masses and dust content for AGN-fitted LRDs. NIRSpec spectra are available for 15 sources, six of which are also in the morphological sample. Broad Hα is detected in 40% (FWHM = 1200–2900 km s^{-1}), and one source shows broad Hβ emission. Emission line ratios indicate a composite nature, consistent with both AGN and stellar processes. Altogether, these results suggest that LRDs are a mixed population, and their rest-frame UV morphology reflects this complexity. Morphological studies of larger samples could provide a new way to understand what drives their properties and evolution.

Unified Astronomy Thesaurus concepts: James Webb Space Telescope (2291); Active galactic nuclei (16); Near infrared astronomy (1093); Galaxy evolution (594); Galaxy formation (595)

1. Introduction

With its unparalleled sensitivity and angular resolution at infrared (IR) wavelengths, JWST (J. P. Gardner et al. 2023) has opened up new frontiers for exploring the early Universe. Not only has it provided the opportunity to study well-known

high-redshift galaxies previously discovered with the Hubble Space Telescope (HST), such as GNz11 (R. J. Bouwens et al. 2010; P. A. Oesch et al. 2016), in much greater detail (e.g., A. J. Bunker et al. 2023; S. Tacchella et al. 2023; R. Maiolino et al. 2024b), but it has also revealed whole populations of high-redshift galaxies (e.g., L. D. Bradley et al. 2023). One of these groundbreaking discoveries is the identification of very compact and red sources, initially reported by I. Labbé et al. (2023b) and subsequently termed "Little Red Dots" (LRDs) by J. Matthee et al. (2024).

These sources are characterized by (1) compactness in the F444W band and (2) a red color at observed wavelengths

---

[21] These authors contributed equally to this work.

greater than ≈ 2 μm covered by the Near Infrared Camera (NIRCam; M. J. Rieke et al. 2023) long-wavelength channel. They exhibit a distinct spectral energy distribution (SED) marked by clear Lyman and Balmer breaks, and a characteristic "v-shaped" continuum in the λ–f_λ plane, i.e., their continua are relatively blue in the rest-ultraviolet but become very red toward the rest-optical. It is worth noting that the location of the "v-shape" feature appears consistently around a rest-frame wavelength of ≈ 3600 Å in sufficiently deep spectroscopic observations (e.g., L. J. Furtak et al. 2024; I. Juodžbalis et al. 2024a; D. J. Setton et al. 2024; B. Wang et al. 2025).

In the very beginning, these sources were reported to exhibit uncomfortably large stellar masses ($M_\star > 10^{10}$ $M_\odot$) with a large amount of dust ($A_V > 1.5$ mag; see I. Labbé et al. 2023b).

Over time, various alternative explanations have been proposed to address these puzzling results. In some cases, the issue could simply arise from an error in the redshift estimation, as demonstrated, e.g., by D. D. Kocevski et al. (2023b) for one of the massive galaxies identified by I. Labbé et al. (2023b) and P. G. Pérez-González et al. (2023a).

Another potential solution explains the high $M_\star$ values by invoking prominent nebular emission, which could mimic the observed red colors at $\lambda > 2$ μm. Recent studies based on JWST observations have indeed shown high-z galaxies with a prominent (Hβ + [O III]) complex and/or Hα emission lines (e.g., R. Endsley et al. 2023, 2024; P. Rinaldi et al. 2023, 2024; K. Boyett et al. 2024; K. I. Caputi et al. 2024). Therefore, if strong emission lines are present, the stellar masses could decrease by a factor of 10, as recently reported by G. Desprez et al. (2024).

Because of their puzzling nature, the discovery of the LRDs has triggered, in less than two years, a vast amount of literature (e.g., L. J. Furtak et al. 2023; M. Killi et al. 2024; V. Kokorev et al. 2023, 2024a, 2024b; I. Labbé et al. 2023a, 2023b; H. Übler et al. 2023; H. B. Akins et al. 2024; G. Barro et al. 2024; E. Durodola et al. 2025; J. E. Greene et al. 2024; K. N. Hainline et al. 2025; E. Iani et al. 2024; D. D. Kocevski et al. 2025; M. Kokubo & Y. Harikane 2024; J. Matthee et al. 2024; P. G. Pérez-González et al. 2024; C. C. Williams et al. 2024), leading to one of the most intriguing questions in extragalactic astronomy today: What is the nature of LRDs?

As observations continue, both photometric and spectroscopic, different groups have tried to unveil the true nature of these red and compact sources. Some of them exhibit broad (≈ 1000 km s^{-1}) Hα emission lines (M. Killi et al. 2024; D. D. Kocevski et al. 2023b; V. Kokorev et al. 2023; J. E. Greene et al. 2024; J. Matthee et al. 2024); therefore, it is widely believed that LRDs could potentially host active galactic nuclei (AGNs). However, their SED model fits can be ambiguous, leaving it unclear whether the emission is primarily driven by an AGN or star formation (G. Barro et al. 2024). It is also possible that LRDs are a mixed population with both AGN and star formation dominated members (e.g., P. G. Pérez-González et al. 2024). Interestingly, P. G. Pérez-González et al. (2024) report that only 17% of their photometrically selected LRDs present broad spectral components.

It has become evident that the Mid-infrared Instrument (MIRI; G. S. Wright et al. 2023) on board JWST could be a game-changer in studying these objects at IR wavelengths, as it could tip the scale in distinguishing between stellar and AGN emission. Noteworthy are several studies in this regard, including those by C. C. Williams et al. (2024) and P. G. Pérez-González et al. (2024), which suggest that these sources could be either dusty starbursts or obscured AGNs. In particular, C. C. Williams et al. (2024), by making use of the Systematic Mid-infrared Instrument Legacy Extragalactic Survey (SMILES; S. Alberts et al. 2024) data, found that the average SED of LRDs flattens beyond 5 μm, indicating the expected turnover of a normal stellar SED at approximately 1.6 μm rest-frame. Building on these findings, P. G. Pérez-González et al. (2024) further concluded that the true nature of LRDs cannot be uniquely described by a single phenomenon, but rather they are likely to be a nonuniform population of objects, with some being extreme starburst galaxies, some dust-obscured AGNs, and some a combination of both.

In this paper, we propose a new approach to advancing our understanding of LRDs. Although these sources are consistently termed "LRDs" due to their selection as red and compact objects in the F444W band from NIRCam, here we focus on their morphology at observed wavelengths shorter than 2 μm, leveraging the superior spatial resolution offered by the NIRCam short-wavelength (SW) channel. Out of a sample of 99 LRDs at $z \approx 4$–8, we find that 30 (30%) are sufficiently extended and have enough signal-to-noise ratio (SNR) per pixel in the rest-frame ultraviolet (UV) for morphological analysis. The remaining 70% appear predominantly compact ($\lesssim$400 pc), likely due to their low SNR in each individual band, which prevents the characterization of any extended components, even when stacking the SW bands. While earlier studies have investigated this subject (e.g., M. Killi et al. 2024; J. F. W. Baggen et al. 2024), ours is the first to apply a statistical approach to address it.

Given that our LRD sample spans $z \approx 4$–8, the NIRCam SW bands trace the UV emission from the galaxies, which can include, for example, star-forming clumps and complexes (e.g., Y. Guo et al. 2015) with strong contributions from massive O-, B-, and A-type stars (see, e.g., R. J. Buta 2011; K. Rubinur et al. 2024), and potentially also the UV continuum emission from an unobscured AGN accretion disk or outflow. This contrasts with the more common morphology studies conducted in the rest-optical, where galaxy-scale asymmetries and strong disturbances are conventionally attributed to merging activity, as this wavelength range primarily traces the emission from relatively evolved stars. We therefore complement the rest-UV morphological analysis where possible with additional data from broadband SEDs and spectroscopy, to place our sample of LRDs in the context of previous studies.

The paper is organized as follows. Section 2 describes the data sets and outlines our sample selection. In Section 3, we explain the methodology for analyzing the UV morphological properties of the selected LRDs. Section 4 presents the SED fitting configuration used to derive stellar properties and discusses these results. In Section 5, we examine the spectral properties of the LRD candidates with NIRSpec spectra, followed by an analysis of the morphology of the LRDs showing broad Balmer lines in Section 6. Finally, Section 7 provides a summary and discussion of our findings.

Throughout this paper, we consider a cosmology with $H_0 = 70$ km s^{-1} Mpc^{-1}, $\Omega_M = 0.3$, and $\Omega_\Lambda = 0.7$. All magnitudes are total and refer to the AB system (J. B. Oke &

J. E. Gunn [1983]). A P. Kroupa ([2001]) initial mass function (IMF) is assumed (0.1–100 $M_\odot$).

2. Data Set and Sample Selection

2.1. Data Set

In this study, we utilized data from both JWST and HST in the GOODS-North and GOODS-South fields (M. Giavalisco et al. [2004]; hereafter GOODS-N and GOODS-S).

2.1.1. NIRCam

We made use of NIRCam data from JADES/NIRCam Data Release 2 (JADES DR2—PIDs: 1180, 1210; PIs: D. Eisenstein and N. Luetzgendorf; D. J. Eisenstein et al. [2023a], [2023b]), which includes observations from the JWST Extragalactic Medium-band Survey (JEMS—PID: 1963; PIs: C. C. Williams, S. Tacchella, and M. Maseda; C. C. Williams et al. [2023]) for GOODS-S and the First Reionization Epoch Spectroscopically Complete Observations (FRESCO—PID: 1895; PI: P. Oesch; P. A. Oesch et al. [2023]) for both GOODS-N and GOODS-S. Additionally, we incorporated NIRCam data from JADES Data Release 3 (DR3) for GOODS-N (F. D'Eugenio et al. [2025]).

The JADES/NIRCam data allow us to cover a wide range of wavelengths ($\approx$1–5 μm). Specifically, the data set in GOODS-N allows us to make use of 11 NIRCam bands (both medium and broad bands; 0.9–4.44 μm), while the data set in GOODS-S allows us to make use of 14 bands (both medium and broad bands; 0.9–4.80 μm).

We estimate a 5σ depth ranging from 30.5 to 30.9 mag (measured in a $0\rlap{.}''2$ radius circular aperture) for the NIRCam data in GOODS-S, highlighting that JADES is one of the deepest NIRCam surveys on the sky.[22] On the other hand, we estimate a 5σ depth ranging from 29.3 to 29.9 mag (measured in a $0\rlap{.}''2$ radius circular aperture) for the NIRCam data in GOODS-N. The total area covered by NIRCam in the GOODS fields is approximately 124 arcmin^2.[23]

2.1.2. HST

For the HST data, we utilized Advanced Camera for Surveys (ACS)/Wide Field Channel (WFC) and WFC3/IR data from the Hubble Legacy Field (HLF) observations that cover both fields, GOODS-N and GOODS-S. The HLF provides deep imaging in nine HST bands covering a wide range of wavelengths (0.4–1.6 μm), from the optical (ACS/WFC F435W, F606W, F775W, F814W, and F850LP filters) to the near-infrared (WFC3/IR F105W, F125W, F140W, and F160W filters). We refer the reader to K. E. Whitaker et al. ([2019]) for a more detailed description of these observations.[24]

2.1.3. NIRSpec

We made use of the Near Infrared Spectrograph's Micro-shutter Array (NIRSpec/MSA; P. Ferruit et al. [2022]; P. Jakobsen et al. [2022]) for the spectroscopic observations from the JADES NIRCam+NIRSpec program (PID: 1181, PI: Eisenstein), which cover the spectral range 0.6–5.3 μm, including observations with both the low-dispersion prism ($R = 30$–300) and all three medium-resolution gratings ($R = 500$–1500). We refer the reader to F. D'Eugenio et al. ([2025]) for a more detailed description of this data set.

2.2. Sample Selection

The ultradeep NIRCam images from JADES in both GOODS-N and GOODS-S enable the photometric selection of red and compact sources, commonly referred to as LRDs, over a total area of $\approx$124 arcmin^2. The extensive data, ranging from HST to NIRCam (the latter also offering medium bands), ensures robustness in photometric redshift estimation (see F. D'Eugenio et al. [2025]; K. N. Hainline et al. [2024]). To select our sample of LRDs in the GOODS fields, we made use of the public JADES DR2/DR3 catalogs. For both our selection and SED fitting, we made use of aperture photometry with $r = 0\rlap{.}''25$ (i.e., CIRC3).

Since the initial identification of red and compact sources by I. Labbé et al. ([2023b]), significant efforts have been made to refine the photometric selection of LRDs. The selection criteria are reasonably effective in identifying broad-line (BL) AGNs. J. E. Greene et al. ([2024]) found that, of the sources followed up spectroscopically, approximately 60% (9/15) were confirmed as BL AGNs. However, 20% of the candidate sources were brown dwarfs, indicating that an additional criterion against this type of contaminant is needed.

The spectra gathered so far of LRDs (e.g., L. J. Furtak et al. [2023]; D. D. Kocevski et al. [2023b]; V. Kokorev et al. [2023]; J. E. Greene et al. [2024]; J. Matthee et al. [2024]) reveal a defining feature: their SEDs appear blue at 1–2 μm (1000–2000 Å rest-frame) and red at 3–5 μm (3100–5200 Å rest-frame), the so-called "v-shape." With this in mind, and following the approach presented in V. Kokorev et al. ([2024a]), we adopt another color criterion (named brown dwarf removal) that can potentially help in reducing the contamination from brown dwarfs, a result based on UNCOVER spectra (see J. E. Greene et al. [2024]).

In addition, compared to the original selection, we relaxed the criterion regarding adjacent filters to avoid excluding potential LRDs due to possible errors in the photometric measurements. Therefore, we visually inspected all selected sources and their SEDs[25] to ensure the inclusion of genuinely red and compact objects, without misclassification due to strong emission lines.

As demonstrated in various studies, using only color criteria can lead to the selection of red sources, whether they are true LRDs (i.e., red and compact) or red and extended. "Compactness" in itself is arbitrary. Therefore, following the example of recent works (e.g., V. Kokorev et al. [2024a]; P. G. Pérez-González et al. [2024]), we included a compactness criterion in the F444W band, which is the band that truly defines these sources as red. Specifically, we adopted the following criterion: F444W($0\rlap{.}''5$)/F444W($0\rlap{.}''25$) < 1.7 (aperture diameters).

Thus, the criteria we adopt in this work are as follows:

1. blue slope: F150W − F200W < 0.8 mag
2. red slope: F277W − F444W > 0.7 mag

---

[22] Only matched in depth (in some bands) by the MIRI Deep Survey/NIRCam-parallel project (P. G. Pérez-González et al. [2023b]) and the Next Generation Deep Extragalactic Exploratory Public Near-infrared Slitless Survey (NGDEEP; M. B. Bagley et al. [2024]).

[23] The JADES data can be downloaded from the following link: https://archive.stsci.edu/hlsp/jades.

[24] The HLF imaging is available at https://archive.stsci.edu/prepds/hlf/.

[25] SEDs come from the official JADES catalog, where EAZY is adopted; see K. N. Hainline et al. ([2024]) for more details.
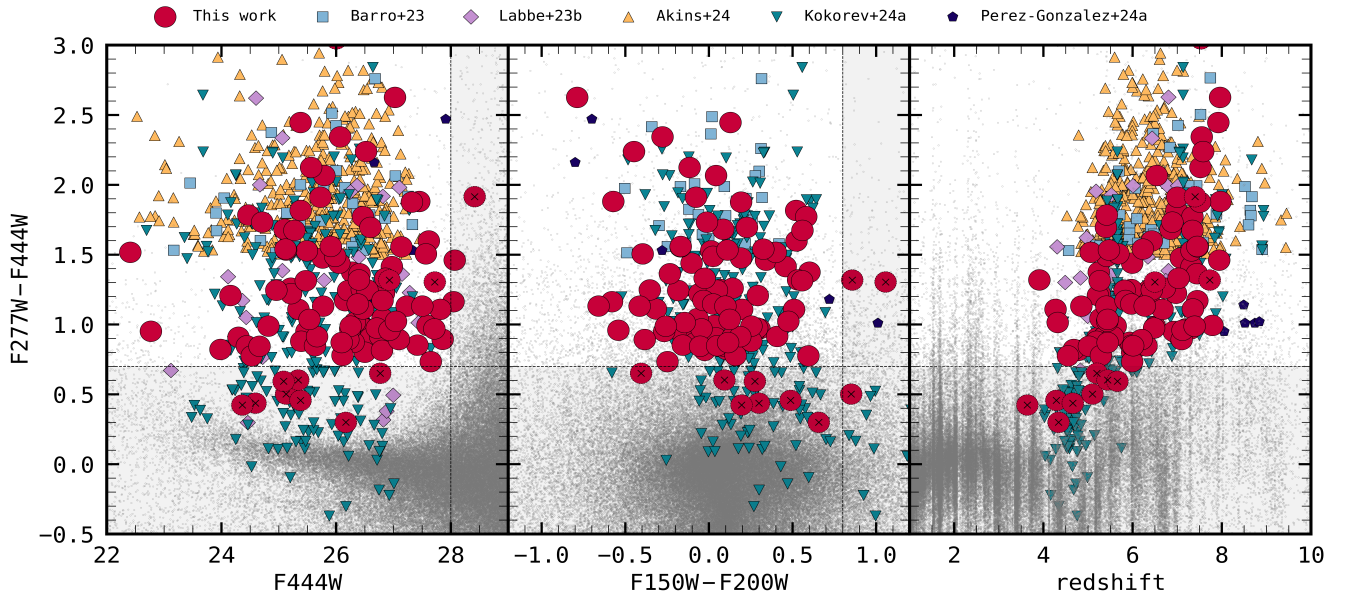
Figure 1. The photometrically selected LRD sample in the GOODS-N and GOODS-S fields at $z \approx 4$–8, alongside other recent literature samples: I. Labbé et al. (2023b), H. B. Akins et al. (2024), G. Barro et al. (2024), V. Kokorev et al. (2024a), and P. G. Pérez-González et al. (2024). Our GOODS-S sample overlaps by 70% with P. G. Pérez-González et al. (2024) and by 75% with V. Kokorev et al. (2024a). The differences arise because P. G. Pérez-González et al. (2024) include sources above $z \approx 8$, which we do not consider in this work, and V. Kokorev et al. (2024a) include sources for which we do not have coverage in both NIRCam/F115W and NIRCam/F200W, preventing us from fully applying our color criteria (see Section 2).

3. `brown dwarf removal`: F115W − F200W > −0.5 mag
4. `compactness`: F444W($0.''5$)/F444W($0.''25$) < 1.7

We then restricted our selection to galaxies with photometric (or spectroscopic) redshifts within the range of ≈ 4–8. This allowed us, for sources with F444W $\lesssim 28$ mag, to probe the UV part of the rest-frame spectrum with the SW bands from NIRCam (probing 0.2 to 0.4 μm at $z \approx 4$ and 0.1–0.2 μm at $z \approx 8$).

By applying the above color and compactness criteria, we initially selected ≈ 350 candidates. After a thorough visual inspection of each source and its SED from EAZY (see K. N. Hainline et al. 2024 for more details), we robustly identified 99 photometrically confirmed LRDs (see Figure 1). This includes 11 sources (marked with a cross) exhibiting LRD-like SEDs that were initially excluded for reasons such as strong emission lines (e.g., the complex Hβ + [O III], which impacts the F277W flux at $z \approx 5.5$ and thus the F277W − F444W color), low SNR in the SW bands, incomplete filter coverage (e.g., GS 206858, which is missing F150W and F200W), or faintness in F444W. These objects were included to account for their red and compact nature. In addition, 15 of our photometrically selected LRDs have NIRSpec spectra. Interestingly, J. Zhang et al. (2025) recently demonstrated that the selection criteria adopted in this work provide a more complete recovery of broad Hα emitters with LRD-like SEDs from NIRCam/WFSS data, compared to the methods used in J. E. Greene et al. (2024) and G. Barro et al. (2024), albeit with a trade-off in purity (see Figure 8 from J. Zhang et al. 2025).

We show our selection in Figure 1 and list the IDs[26] and coordinates in Table 1. In Figure 2, we present two examples of our selected LRDs, where we show the comparison between the NIRCam SW red, green, and blue (RGB; F090W, F115W, and F200W) and the "classic" RGB (F090W, F277W, and F444W). This simple visual comparison reveals that LRDs can exhibit complex morphologies in UV light, suggesting that they might not be just a dot.

We cross-matched our sample with existing AGN catalogs in GOODS-S and GOODS-N. None of our sources appear in the pre-JWST AGN catalogs (J. Lyu et al. 2022), which is expected given their limited coverage of high-redshift sources. However, six of our sources are included in the MIRI AGN catalog presented by J. Lyu et al. (2024). Among these, four have photometric redshifts consistent with those reported in J. Lyu et al. (2024), while the remaining two have uncertain redshift estimates. Interestingly, four LRDs (GS 197348, GN 1001093, GN 1061888, and GN 1010816) were also identified in R. Maiolino et al. (2024a) and A. J. Bunker et al. (2024). The AGN classification carried out in J. Lyu et al. (2024) is primarily based on a significant MIRI photometric excess, consistent with hot dust emission from an obscured torus. While such a rising IR SED is atypical for the average LRD population, which often exhibits a flattening beyond 1 μm (e.g., C. C. Williams et al. 2024), it is important to note that relying on average SEDs may overlook the intrinsic heterogeneity within this class. In this context, P. G. Pérez-González et al. (2024) demonstrated that when MIRI data are included, photometrically selected LRDs display a broad range of behaviors, with some SEDs flattening and others rising, highlighting the diverse nature of the population. It is also worth mentioning that two notable sources follow the average LRD shape but exhibit a rising IR SED: the Rosetta Stone from I. Juodžbalis et al. (2024a) and Virgil from E. Iani et al. (2025) and P. Rinaldi et al. (2025).

[26] Throughout the paper, we refer to sources by their NIRCam IDs for simplicity.

Table 1
List of Photometrically Selected LRDs in the GOODS Fields

JADES ID	NIRCam ID	Redshift	R.A. (deg)	Decl. (deg)	JADES ID	NIRCam ID	Redshift	R.A. (deg)	Decl. (deg)
JADES-GN+189.1797+62.2246	1001093	5.595*	189.1797	62.2246	JADES-GS+53.0763-27.9099	2532	6.98	53.0763	−27.9099
JADES-GN+189.0915+62.2281	1001830	6.675*	189.0915	62.2281	JADES-GS+53.1191-27.8926	11786	7.34	53.1191	−27.8926
JADES-GN+189.1096+62.2285	1001895	7.52	189.1096	62.2285	JADES-GS+53.1072-27.8906	13418	6.50	53.1072	−27.8906
JADES-GN+189.1277+62.2326	1002836	7.10	189.1277	62.2326	JADES-GS+53.1136-27.8848	19348	5.41	53.1136	−27.8848
JADES-GN+189.0963+62.2391	1004685	7.414*	189.0963	62.2391	JADES-GS+53.0570-27.8744	35453	5.10	53.0570	−27.8744
JADES-GN+189.1517+62.2594	1010767	6.20	189.1517	62.2594	JADES-GS+53.0641-27.8709	39376	7.00	53.0641	−27.8709
JADES-GN+189.1520+62.2596	1010816	6.759*	189.1520	62.2596	JADES-GS+53.0558-27.8690	41769	7.79	53.0558	−27.8690
JADES-GN+189.2038+62.2684	1013041	7.089*	189.2038	62.2684	JADES-GS+53.1304-27.8607	54648	6.37	53.1304	−27.8607
JADES-GN+189.0571+62.2689	1013188	7.32	189.0571	62.2689	JADES-GS+53.1153-27.8592	57356	4.27	53.1153	−27.8592
JADES-GN+189.0385+62.2693	1013282	7.12	189.0385	62.2693	JADES-GS+53.1083-27.8510	70714	6.50	53.1083	−27.8510
JADES-GN+189.0659+62.2733	1014361	4.32	189.0659	62.2733	JADES-GS+53.0605-27.8484	73690	5.40	53.0605	−27.8484
JADES-GN+189.0721+62.2734	1014406	5.19	189.0721	62.2734	JADES-GS+53.1476-27.8420	79803	5.41	53.1476	−27.8420
JADES-GN+189.0506+62.2794	1016275	7.97	189.0506	62.2794	JADES-GS+53.1127-27.8383	82737	5.21	53.1127	−27.8383
JADES-GN+189.0577+62.2836	1017514	5.02	189.0577	62.2836	JADES-GS+53.0732-27.8331	86916	7.05	53.0732	−27.8331
JADES-GN+189.0612+62.2841	1017694	7.34	189.0612	62.2841	JADES-GS+53.1281-27.8292	89635	5.99	53.1281	−27.8292
JADES-GN+188.9878+62.2911	1020140	4.66	188.9878	62.2911	JADES-GS+53.1338-27.8283	90354	7.96	53.1338	−27.8283
JADES-GN+189.1131+62.2924	1020485	5.26	189.1131	62.2924	JADES-GS+53.1590-27.8183	99267	6.67	53.1590	−27.8183
JADES-GN+189.1590+62.2602	1029154	5.62	189.1590	62.2602	JADES-GS+53.1593-27.8117	104238	5.28	53.1593	−27.8117
JADES-GN+189.0409+62.2693	1030265	5.42	189.0409	62.2693	JADES-GS+53.1019-27.8109	104849	5.24	53.1019	−27.8109
JADES-GN+189.1798+62.2824	1032447	7.086*	189.1798	62.2824	JADES-GS+53.1408-27.8022	110739	5.916*	53.1408	−27.8022
JADES-GN+189.0870+62.2908	1033797	5.22	189.0870	62.2908	JADES-GS+53.1254-27.7874	120484	7.08	53.1254	−27.7874
JADES-GN+189.1983+62.2970	1034762	7.043*	189.1983	62.2970	JADES-GS+53.1269-27.7862	121710	7.92	53.1269	−27.7862
JADES-GN+189.2586+62.1432	1037138	7.51	189.2586	62.1432	JADES-GS+53.1728-27.7831	124327	7.94	53.1728	−27.7831
JADES-GN+189.2395+62.1444	1037341	5.68	189.2395	62.1444	JADES-GS+53.2040-27.7721	132229	7.247*	53.2040	−27.7721
JADES-GN+189.2346+62.1475	1037974	7.46	189.2346	62.1475	JADES-GS+53.1908-27.7679	136872	7.19	53.1908	−27.7679
JADES-GN+189.2707+62.1484	1038147	5.82	189.2707	62.1484	JADES-GS+53.1479-27.7599	143133	6.43	53.1479	−27.7599
JADES-GN+189.2062+62.1505	1038673	6.43	189.2062	62.1505	JADES-GS+53.1582-27.7391	154428	6.54	53.1582	−27.7391
JADES-GN+189.2631+62.1512	1038849	3.91	189.2631	62.1512	JADES-GS+53.0789-27.8842	165902	5.56	53.0789	−27.8842
JADES-GN+189.2940+62.1531	1039353	5.29	189.2940	62.1531	JADES-GS+53.0877-27.8712	172975	4.78	53.0877	−27.8712
JADES-GN+189.2436+62.1549	1039805	5.26	189.2436	62.1549	JADES-GS+53.0557-27.8688	174121	7.30	53.0557	−27.8688
JADES-GN+189.2024+62.1627	1042541	5.41	189.2024	62.1627	JADES-GS+53.0374-27.8656	175930	5.35	53.0374	−27.8656
JADES-GN+189.3216+62.1627	1042550	7.45	189.3216	62.1627	JADES-GS+53.0964-27.8531	184838	7.32	53.0964	−27.8531
JADES-GN+189.2735+62.1665	1043804	5.84	189.2735	62.1665	JADES-GS+53.1060-27.8482	187025	6.92	53.1060	−27.8482
JADES-GN+189.3395+62.1848	1050323	6.89	189.3395	62.1848	JADES-GS+53.1265-27.8181	197348	5.919*	53.1265	−27.8181
JADES-GN+189.1748+62.1901	1052210	6.01	189.1748	62.1901	JADES-GS+53.0677-27.8123	198980	4.68	53.0677	−27.8123
JADES-GN+189.1493+62.2075	1058594	3.64	189.1493	62.2075	JADES-GS+53.1548-27.8065	200576	6.31	53.1548	−27.8065
JADES-GN+189.1680+62.2170	1061888	5.874*	189.1680	62.2170	JADES-GS+53.1214-27.7949	203749	7.53	53.1214	−27.7949
JADES-GN+189.2248+62.2258	1064405	5.20	189.2248	62.2258	JADES-GS+53.1135-27.7935	204022	7.45	53.1135	−27.7935
JADES-GN+189.2613+62.2320	1065744	5.56	189.2613	62.2320	JADES-GS+53.1386-27.7903	204851	5.42	53.1386	−27.7903
JADES-GN+189.2292+62.1462	1068797	5.06	189.2292	62.1462	JADES-GS+53.1390-27.7844	206858	3.941*	53.1390	−27.7844
JADES-GN+189.2141+62.1490	1069100	5.44	189.2141	62.1490	JADES-GS+53.1661-27.7720	210600	6.310*	53.1661	−27.7720
JADES-GN+189.2793+62.1501	1069299	5.47	189.2793	62.1501	JADES-GS+53.1792-27.7587	214552	5.97	53.1792	−27.7587
JADES-GN+189.2358+62.1681	1072112	5.43	189.2358	62.1681	JADES-GS+53.1925-27.7531	216165	5.99	53.1925	−27.7531
JADES-GN+189.1974+62.1772	1073488	4.132*	189.1974	62.1772	JADES-GS+53.1848-27.7440	217926	6.97	53.1848	−27.7440
JADES-GN+189.3075+62.1780	1073625	6.23	189.3075	62.1780	JADES-GS+53.1583-27.7409	218515	5.98	53.1583	−27.7409
JADES-GN+189.1786+62.1872	1075363	5.44	189.1786	62.1872	JADES-GS+53.1614-27.7377	219000	6.85	53.1614	−27.7377
JADES-GN+189.1493+62.2083	1079572	3.966*	189.1493	62.2083	JADES-GS+53.1248-27.8663	283663	4.55	53.1248	−27.8663

Table 1
(Continued)

JADES ID	NIRCam ID	Redshift	R.A. (deg)	Decl. (deg)	JADES ID	NIRCam ID	Redshift	R.A. (deg)	Decl. (deg)
JADES-GN+189.2816+62.2161	1081040	4.85	189.2816	62.2161	⋯	⋯	⋯	⋯	⋯
JADES-GN+189.2854+62.2235	1081928	6.27	189.2854	62.2235	⋯	⋯	⋯	⋯	⋯
JADES-GN+189.0962+62.2392	1113205	7.40	189.0962	62.2392	⋯	⋯	⋯	⋯	⋯
JADES-GN+189.2143+62.1491	1119051	5.44	189.2143	62.1491	⋯	⋯	⋯	⋯	⋯
JADES-GN+189.1364+62.2226	1177425	7.03	189.1364	62.2226	⋯	⋯	⋯	⋯	⋯

Note. Sources with spectroscopic redshifts (z_{spec}) are marked with [*] (A. J. Bunker et al. 2023; F. D'Eugenio et al. 2025). Photometric redshifts come from EAZY (K. N. Hainline et al. 2024).
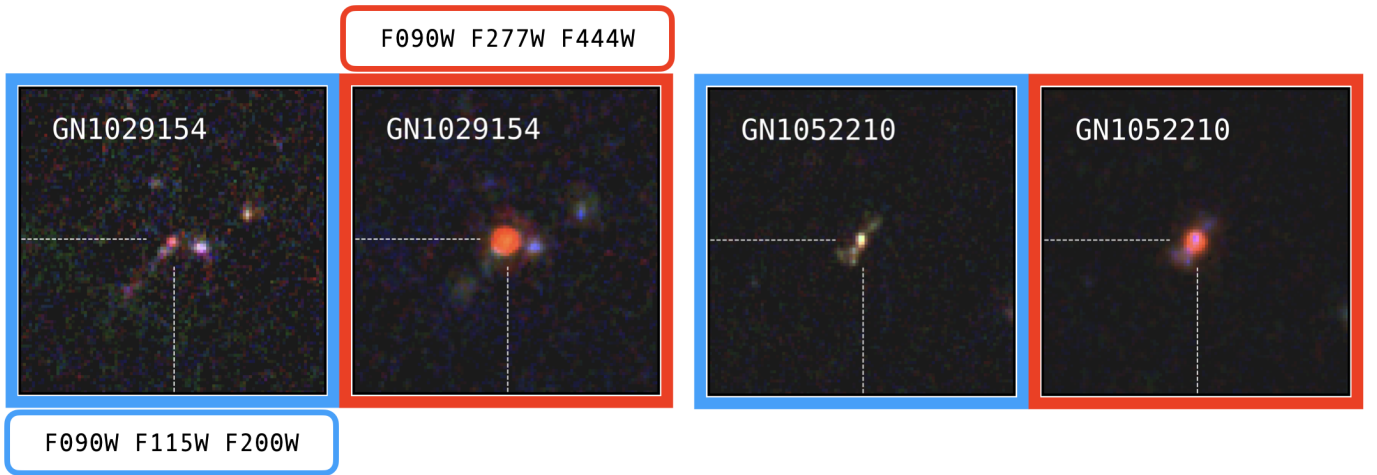
Figure 2. We display two examples from our sample of 99 photometrically selected LRDs in the GOODS-N and GOODS-S fields. For each source, we present two sets of $3'' \times 3''$ RGB postage stamps: one using the SW bands (F090W, F115W, and F200W) and another with the classic RGB colors (F090W, F277W, and F444W). A visual comparison between these two sets reveals that for these two sources—which also have high SNR in the NIRCam SW bands—the morphology appears more complex at the shorter wavelengths compared to the classic compact morphology typically associated with LRDs at longer wavelengths (as highlighted in the classic RGB, in red), suggesting that they are not just a dot.

3. LRD Morphology

3.1. Morphological Analysis: STATMORPH

To study the UV morphology of the LRDs in our sample, we made use of the STATMORPH (V. Rodriguez-Gomez et al. 2019) software, which computes a variety of morphology measures on an input image of a galaxy. To prepare image cutouts for input to the code, for each LRD we generated a $3'' \times 3''$ image with a pixel scale of $0\overset{''}{.}03\ \mathrm{px}^{-1}$,[27] stacked over the point-spread function (PSF)-matched[28] SW filters to maximize the SNR and ensure meaningful morphological measurements (a STATMORPH measure of >2.5 SNR/pixel in the source aperture is considered to be reliable; refer to V. Rodriguez-Gomez et al. 2019 for details). The image stacking also allowed us to identify the subset definitively showing extended structure and/or multiple apparently associated sources beyond the size of the SW FWHM. Out of 99 photometrically selected LRDs in GOODS-S and GOODS-N, we find that 30 LRDs in total display clear morphological features (both on the single SW images and on the stacked SW bands), while the remaining 69 appear predominantly compact, lacking a sufficient SNR for detailed characterization of any extended components, even when stacking the images. After verifying that the resulting subsample of 30 extended LRDs were detected with sufficient SNR/pixel values for analysis (in the range 4.8–12.8), we computed their nonparametric morphological measurements. From the suite of morphology indicators calculated by STATMORPH, we chose to utilize the nonparametric multi-mode–intensity–deviation (MID) statistics (P. E. Freeman et al. 2013) and the shape asymmetry (A_S) parameter (M. M. Pawlik et al. 2016).

3.1.1. MID and Shape Asymmetry (A_S) Statistics

The MID statistics are useful for detecting multicomponent systems, such as the double nucleus of a late-stage merger, highly disordered postmerger remnants, galaxies with bright star-forming clumps in rest-UV emission, or an apparently single galaxy with an extended emission component(s). Briefly, the multimode (M) statistic identifies all noncontiguous groups of image pixels above a given intensity threshold and computes the area ratio of the top two largest regions. The intensity (I) statistic complements M by calculating the intensity ratio between the two brightest regions in the galaxy image. Finally, the distance (D) statistic measures the normalized distance between the brightest local intensity maximum in the galaxy image and the centroid of the total emission, as identified in the binary detection mask (i.e., segmentation map). A more detailed explanation of these statistics can be found in Appendix B. The A_S parameter is a variation of the classic asymmetry parameter (A) in that it is calculated using the binary detection mask as opposed to the flux image (M. M. Pawlik et al. 2016). The A_S parameter was designed in this way to detect the faint disturbances that appear along the edges of a galaxy merger remnant, such as wisps, cusps, and tidal tails, as well as the overall spatial asymmetry that characterizes an early- or late-stage merger as a singular system. In fact, R. Nevin et al. (2019) show A_S to be the single most important nonparametric diagnostic of merger morphology in imaging data, over a maximal length of the merger lifetime.

P. E. Freeman et al. (2013) demonstrate that the MID statistics in combination with the classic asymmetry parameter (A) represent the most important set of nonparametric morphology indicators for accurately recovering known galaxy classifications,[29] and do not

---

[27] For GOODS-S and GOODS-N, we adopted the following filters: F090W, F115W, F150W, F182M, F200W, and F210M. However, we caution that not all these bands were available for every source in our sample due to incomplete coverage in certain filters (e.g., in GOODS-S, F182M and F210M are only available from FRESCO and JEMS data).

[28] Before performing the morphological analysis with STATMORPH on the stacked galaxy image cutouts, we PSF-matched all NIRCam SW bands to the reddest available band for each galaxy. Interestingly, a comparison of the STATMORPH results before and after PSF matching shows that the overall conclusions remain unchanged, further reinforcing the intrinsically complex UV morphology of these sources, as independently suggested in other studies (e.g., C.-H. Chen et al. 2025).

[29] While the extensively studied concentration–asymmetry–smoothness (CAS; C. J. Conselice et al. 2003) and Gini–M_{20} (GM_{20}; J. M. Lotz et al. 2004) morphology diagnostics are also computed by STATMORPH, the reliability of these statistics is known to decrease with decreasing galaxy size and SNR. Therefore, given the compact sizes and high redshift of LRDs, we utilized instead the (MID) statistics that were introduced in P. E. Freeman et al. (2013) as an alternative to CAS and GM_{20} when such criteria hold.
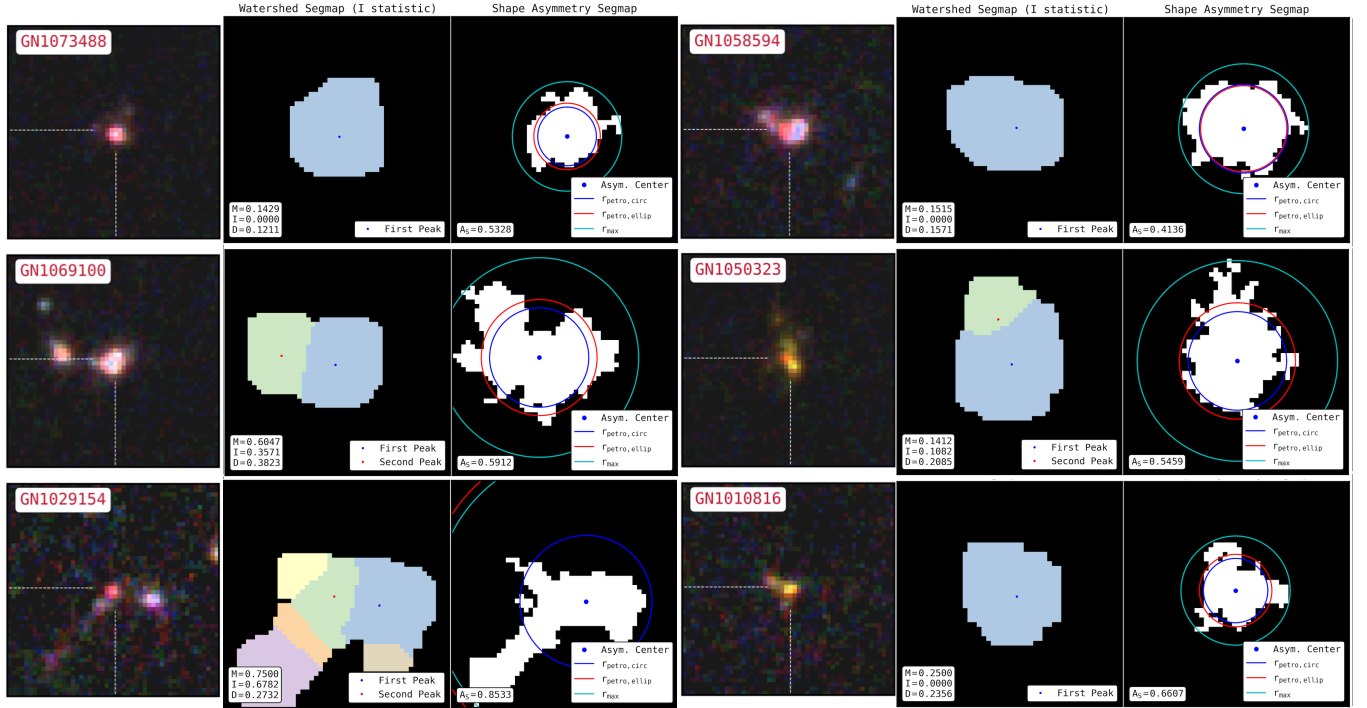
Figure 3. Example STATMORPH output images (middle and rightmost images in each image triplet) along with the associated SW RGB image of galaxy emission (leftmost image), showing the resulting MID and A_S values that constitute our quantitative LRD morphology study. The middle image of each source image triplet shows the segmentation map used specifically to calculate the I statistic, where each distinct intensity maximum is highlighted with a different color. The sources with a single (blue) region represent single sources of emission; however 87% of them show nonzero M statistic values, indicating that the spatial footprints of multiple distinct source regions were detected (see Section 3 and the appendix for a discussion of the M and I statistics). In the galaxy segmentation image used to calculate shape asymmetry, contained within the r_{max} aperture (cyan line), A_S values greater than 0.2 mark a strong asymmetry/disturbance. It can be seen from the representative LRD examples shown here that they present highly asymmetric and complex morphologies, including systems with multiple sources, irregularly shaped single sources with multiple distinct regions of emission, and bright pointlike sources embedded in fainter extended emission.

show any systematic variation with galaxy size, degree of elongation, or SNR (at SNR $\gtrsim$ 1.7). However, given the unreliability of A in instances of relatively low SNR and resolution (e.g., C. J. Conselice et al. 2003), as well as its inability to distinguish mergers from nonmergers over a significant fraction of the merger lifetime, we utilized the A_S parameter instead, which outperforms A in each of these instances (R. Nevin et al. 2019).

The detailed algorithmic descriptions of these nonparametric morphology indicators are presented in the appendix.

3.2. The UV Morphological Properties of the LRDs

In Figure 3, we show the STATMORPH results of the MID and A_S statistic computation for a representative subset of the 30 LRDs in our sample appearing as multiple associated sources, irregularly shaped single sources, and apparent point sources embedded in fainter extended emission. In each triplet of images shown per source, the statistic values are displayed along with the corresponding segmentation map used in the calculation of each (P. E. Freeman et al. 2013; M. M. Pawlik et al. 2016; V. Rodriguez-Gomez et al. 2019). Figure 4 shows the measured relationship between A_S and the MID statistic values, which reveals that all LRDs included in the morphological analysis appear as strongly spatially disturbed systems, independently of the number of distinct sources or emission components detected, as indicated by A_S values greater than 0.2 (M. M. Pawlik et al. 2016). It can also be seen that A_S is positively correlated with the corresponding nonzero (i.e., multicomponent) M and I values, as expected where multiple components of emission are

detected within/around the source (P. E. Freeman et al. 2013; see appendix for details). Furthermore, the nonzero M and I statistic values are also positively correlated with one another, showing that the spatial area and brightness of a detected secondary source of emission tend to grow in tandem. The resulting values for the M and I statistics in our LRD sample show strong cases for multiple associated sources where their values tend toward 1, suggestive of a major merger, as well as candidates for minor mergers where the values are smaller (or one or more significant clumps of UV emission associated with a single source).

For the $\approx$50% of cases with zero I values (only one intensity peak identified in the galaxy emission) but nonzero M values (multiple noncontiguous pixel groups identified above a given intensity threshold), it is clear from visual inspection that these represent LRDs with a single galaxy attached to an extended asymmetric emission structure. Finally, only in two cases do we find both zero I and M statistic values (i.e., a single and coincident spatial and emission component). However, both of these sources exhibit an asymmetric/disturbed spatial imprint, one with an A_S value indicative of a mild spatial disturbance, and the other, of a strong disturbance. However, these two LRDs show particularly small sizes and relatively lower SNRs compared to the rest of the sample examined in the morphological analysis, making it possible that they have multiple components that evaded detection by M and I.

Given that the D statistic provides an independent measure of galaxy asymmetry (see appendix) and therefore serves as a nonredundant complement to A_S, we observe these two
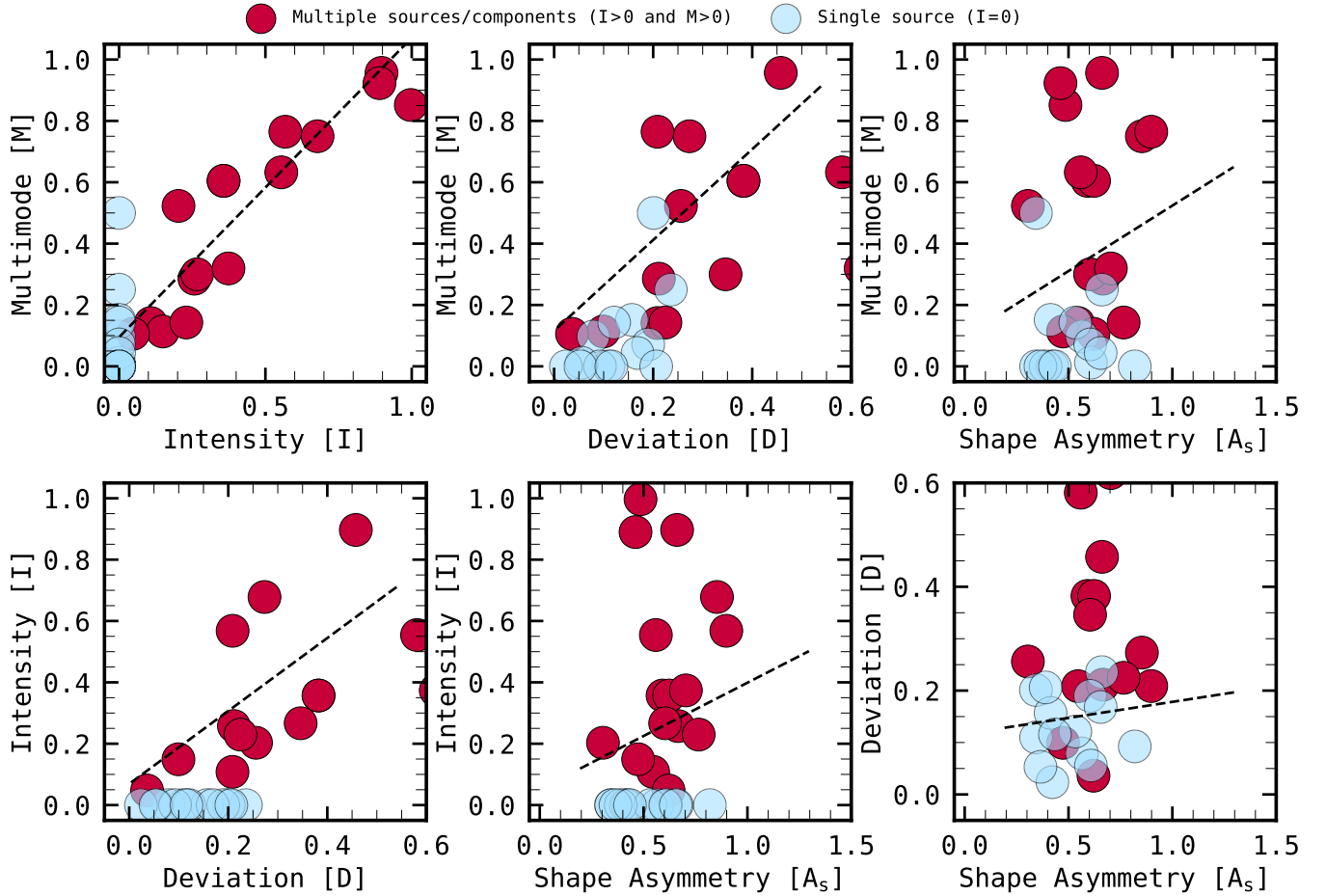
Figure 4. An adaptation of Figure 5 in P. E. Freeman et al. (2013), where the MID statistics for measuring galaxy morphologies are introduced, but with the classic asymmetry parameter, A, replaced by the shape asymmetry parameter, A_S; see Section 3.1. The red symbols are akin to the merger candidates in the referenced work, as they represent the LRDs in our sample exhibiting multiple distinct emission and spatial components (indicated by nonzero I and M values, respectively). Close pairs of sources with similar brightnesses and sizes, such as major-merger candidates, would show I and M values tending toward a value of 1, while lower values of these two statistics would suggest a minor-merger candidate, or a single source with a relatively small and faint "companion" UV clump of emission. The blue symbols represent those LRDs identified with only a single ($I = 0$), asymmetric ($A_S > 0.2$) source of emission, with most (87%) showing multiple noncontiguous pixel regions by their nonzero M statistic values (similar to the "nonregular" nonmerger candidates in P. E. Freeman et al. 2013). In short, all of the LRDs examined in the morphological analysis display irregular and extended features. The black lines represent the fit to the multisource/multicomponent LRDs (red points), demonstrating the expected positive linear relationship between these statistics. Based on the random forest regression and classification analysis of the combined MID and A statistics measured for 1639 galaxies in HST/WFC3 H- and J-band images in P. E. Freeman et al. (2013), both the visually labeled (red) multicomponent systems (classified as purely mergers in their study) and the (blue) nonmerging irregular galaxies are detected with ≈78% accuracy (i.e., the percentage of correctly classified nonregular or merging galaxies).

parameters to positively correlate, as expected, in instances where the LRD appears significantly extended, noncentralized, and disturbed. Furthermore, where a source happens to show a relatively symmetric spatial outline in the A_S binary detection mask with equally weighted pixel values (tending toward lower values of A_S), D can still indicate a relatively high level of disturbance/disorder within the brightness distribution of the corresponding flux image of the galaxy, such as in the observed cases of an extended single source, but with its brightest peak of emission appearing off-center.

In Table 2, we summarize the main LRD properties estimated with STATMORPH. The MID statistics indicate that 50% of the LRDs selected for morphological analysis show at least two distinct, apparently associated sources or galaxy components, with the remainder appearing as single sources with highly asymmetric structure. We also notice from M and I that in ≈50% of the multicomponent LRDs, the two sources/regions used in the calculation of each statistic are of comparable brightness and size, suggesting they are potential major-merger candidates in

the pre-merger or late-stage phase. To test whether the multiple components of the merger candidates are physically associated, we examined photometric redshifts and, where available, spectroscopic redshifts from NIRCam/WFSS observations (FRESCO and CONGRESS; P. A. Oesch et al. 2023; X. Lin et al. 2025). For apparent companions with reliably extracted photometry, we find redshifts consistent with those of the LRDs, supporting a physical association rather than a chance projection. In cases where the companions are extremely close, reliable photometry is more difficult to obtain. However, aperture photometry within small radii often has an SED shape consistent with that of the central LRD, further suggesting a potential physical connection, though firm conclusions remain uncertain.

4. LRD Stellar Properties

4.1. SED Fitting: BAGPIPES

We used BAGPIPES (A. C. Carnall et al. 2019) to perform SED fitting and derive the stellar properties of the 99

Table 2
Morphological Parameters for the LRDs with Enough SNR for Morphological Analysis

NIRCam ID	$r_{\mathrm{max,circ}}$	SNR/pixel	A_{S}	M	I	D
11786	6.315	3.483	0.661	0.957	0.897	0.458
13418	4.736	6.932	0.620	0.106	0.048	0.036
19348	3.127	6.876	0.390	0.000	0.000	0.206
79803	5.376	10.515	0.461	0.923	0.890	0.631
172975	4.164	13.419	0.604	0.071	0.000	0.190
174121	6.434	9.504	0.604	0.300	0.267	0.346
175930	5.230	44.287	0.819	0.000	0.000	0.093
187025	4.982	14.451	0.655	0.043	0.000	0.168
197348	14.825	12.124	0.704	0.319	0.374	0.619
204851	14.683	8.208	0.485	0.852	0.997	0.776
206858	14.244	13.344	0.559	0.632	0.554	0.581
210600	5.292	15.948	0.365	0.000	0.000	0.053
214552	8.968	6.201	0.765	0.143	0.230	0.225
219000	3.726	24.490	0.434	0.000	0.000	0.116
1010816	5.758	6.466	0.661	0.250	0.000	0.236
1017514	4.615	9.338	0.343	0.500	0.000	0.201
1020140	4.578	13.954	0.344	0.000	0.000	0.110
1029154	14.055	5.502	0.853	0.750	0.678	0.273
1033797	4.364	4.478	0.564	0.098	0.000	0.079
1038147	4.549	22.171	0.608	0.012	0.000	0.056
1050323	8.081	10.632	0.546	0.141	0.108	0.209
1052210	8.159	15.250	0.474	0.114	0.149	0.099
1058594	7.587	22.272	0.414	0.152	0.000	0.157
1065744	4.562	15.248	0.422	0.000	0.000	0.024
1069100	9.045	27.571	0.591	0.605	0.357	0.382
1069299	23.252	7.181	0.666	0.286	0.258	0.211
1073488	4.978	18.402	0.533	0.143	0.000	0.121
1079572	22.575	3.778	0.898	0.765	0.568	0.209
1081040	15.603	8.041	0.304	0.523	0.203	0.256
1119051	9.138	27.570	0.623	0.605	0.357	0.382

Note. This table lists the morphological parameters extracted from STAT-MORPH for the LRDs with sufficient SNR for robust morphological analysis. Columns include the maximum circular radius $r_{\mathrm{max,circ}}$, SNR per pixel, shape asymmetry (A_{S}), multiplicity (M), intensity (I), and deviation (D).

photometrically selected LRDs. For the 15 galaxies with available spectroscopy, we also performed joint spectro-photometric fitting. In all cases, the redshift was fixed, based on either the photometric or spectroscopic values.

BAGPIPES relies on synthetic templates from G. Bruzual & S. Charlot (2003) with a P. Kroupa (2001) IMF, adopting a cutoff mass of 100 $M_{\odot}$, and nebular emission modeled with CLOUDY (G. J. Ferland et al. 2013). We employed a continuity nonparametric star formation history model (J. Leja et al. 2019). For the latter, we defined the age bin edges (counted in lookback time from the redshift of the observation) based on each source's redshift (photometric or spectroscopic), following a logarithmic distribution from $z = 30$ to the age of the Universe at that redshift. We adopted the same approach for the age parameter. Stellar masses were allowed to range between 10^5 and 10^{13} $M_{\odot}$ (uniform prior in log). We opted for a Calzetti reddening law (D. Calzetti et al. 2000), allowing A_V to vary between 0 and 6, and allowed metallicity ($Z/Z_{\odot}$) to range from 0 to 2.5. The ionization parameter (U) was fixed at -2. Finally, each fit was calculated twice, with and without invoking an AGN component. We adopted the AGN implementation provided in BAGPIPES, which models the continuum as a two-slope power law and includes broad Gaussian emission lines for Hα and Hβ, following the

approach of A. C. Carnall et al. (2023; see their Table 1). This model is sufficient to account for potential AGN contributions when estimating stellar properties, which is the main goal of this section. A detailed analysis of the AGN nature is presented in Section 5, based on the available NIRSpec spectra.

For the sources with NIRSpec spectra, we followed the techniques described by A. C. Carnall et al. (2019) to fully leverage the combination of spectroscopic and photometric data. As outlined in R. Navarro-Carrera et al. (2024), we allowed for a $<2\sigma$ perturbation to the spectrum using a second-order Chebyshev polynomial to correct for systematic uncertainties in flux calibration. Additionally, we allowed for a multiplicative factor on the spectroscopic errors to correct for underestimated uncertainties.

4.2. Results

For runs allowing AGNs, we find that our LRDs have an average $A_V = 2.74^{+0.55}_{-0.71}$ mag (16th and 84th percentiles), consistent with the original results from I. Labbé et al. (2023b), where their sample of red, compact sources exhibited $A_V > 1.5$ mag. This also aligns with the recent findings from H. B. Akins et al. (2024), who identified a large population of red, compact objects in COSMOS. Our sources show, on average, $\log_{10}(M_\star/M_\odot)=9.67^{+0.17}_{-0.27}$ (16th and 84th percentiles), in agreement with the recent literature about LRDs (e.g., H. B. Akins et al. 2024; see the left panel in Figure 5). On the other hand, the BAGPIPES run using only stellar models indicates that our LRDs have, on average, $A_V = 1.16^{+0.11}_{-0.21}$ mag (16th and 84th percentiles) and an average $\log_{10}(M_\star/M_\odot) = 9.07^{+0.11}_{-0.08}$ (16th and 84th percentiles). To first order the lower $M_\star$ is a reflection of the lower extinction. These masses may, of course, be overestimated if the galaxies have IMFs that are more top-heavy than the Kroupa one used in BAGPIPES.

Some sources in our sample exhibit very high $M_\star$, consistent also with the runs using stellar models alone. To interpret this, we estimate their implied star formation efficiency ε, defined as the fraction of baryons within a halo that are converted into stars, i.e., $\varepsilon = M_\star/(f_{\mathrm{b}} M_{\mathrm{halo}})$, where $f_{\mathrm{b}} = 0.156$ is the cosmic baryon fraction from Planck and M_{halo} is the host halo mass inferred from abundance matching at fixed comoving number density (see also M. Boylan-Kolchin 2023). We calculate the stellar mass ceiling corresponding to a maximal efficiency $\varepsilon = 1$ and a more typical upper bound $\varepsilon = 0.2$ by computing the cumulative halo mass function over the JADES survey area (GOODS-S + GOODS-N).[30]

We find that a small number of galaxies in our sample lie above the $\varepsilon = 1$ limit computed for the JADES area, similar to findings from the COSMOS-Web field by H. B. Akins et al. (2024). Two sources, which have NIRSpec spectra, show $\log_{10}(M_\star/M_\odot) > 10$ at $z \approx 6.5-7.5$ and sit at $\varepsilon > 0.2$. While one spectrum is of poor quality, the other (GN 1010816) is robust and confirms a very high stellar mass of $\log_{10}(M_\star/M_\odot) = 10.62^{+0.05}_{-0.05}$ at $z_{\mathrm{spec}} = 6.759$. Although such massive galaxies are expected to be rare at these redshifts, the implied star formation efficiencies challenge standard assumptions about baryon conversion and may point to alternative scenarios or underestimated halo masses. The BAGPIPES fit for this object is shown in Figure 6, illustrating how the

---
[30] We made use of the Python package hmf and halomod (S. G. Murray et al. 2013) that can be found here: https://github.com/halomod. We adopted an SMT fitting function (R. K. Sheth et al. 2001).
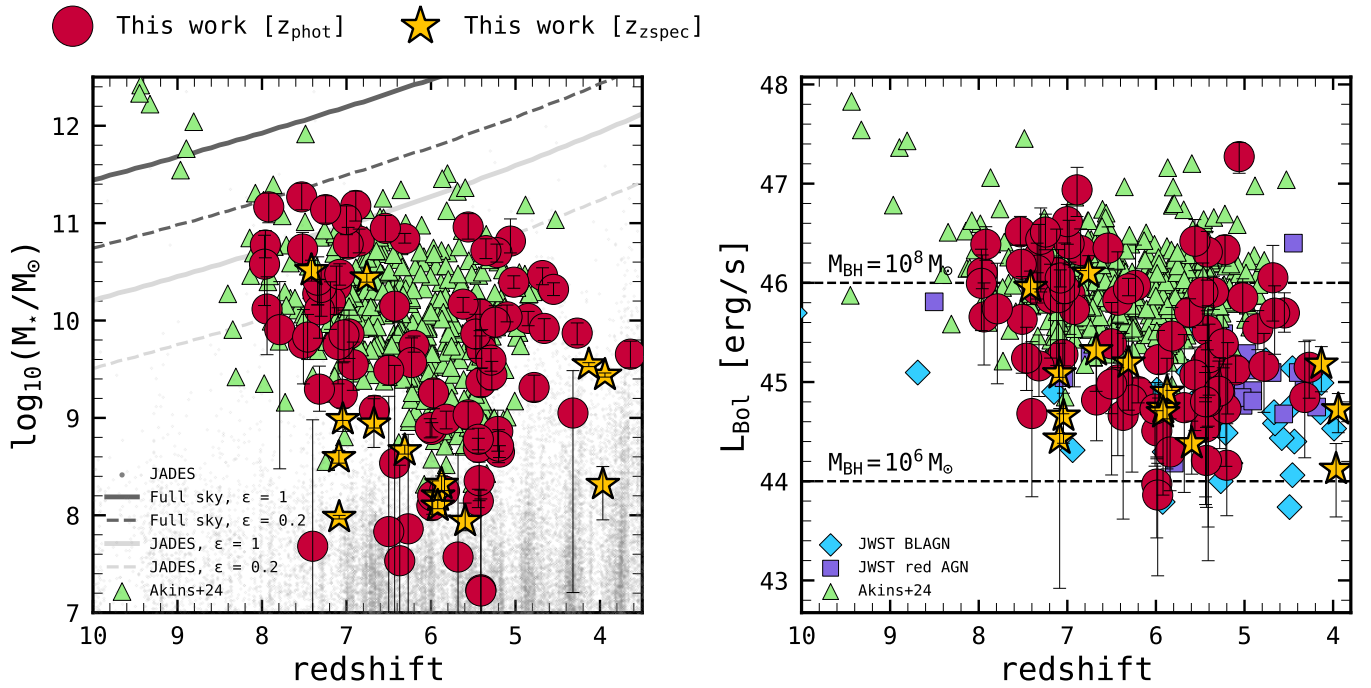
Figure 5. Left panel: $M_\star$ as a function of redshift for our sample of 99 photometrically selected LRDs in the GOODS fields. In this plot, $M_\star$ comes from the BAGPIPES runs with AGNs. No significant differences arise when plotting $M_\star$ adopting stellar models only. Gray points represent galaxies from JADES DR2/DR3. The large sample of LRDs from H. B. Akins et al. (2024) is presented for comparison. The sources with spectra are denoted by yellow stars. Gray points represent the JADES sources in both GOODS-S and GOODS-N. The allowed $M_\star$ as a function of redshift for two different star formation efficiency values are also shown for the JADES area and the full sky. Right panel: L_{Bol} as a function of redshift. We computed L_{Bol} from the intrinsic model SED (i.e., before any dust attenuation) by using the monochromatic luminosity at 5100 Å and a bolometric correction of 9 (G. T. Richards et al. 2006). For comparison, we plot the LRD sample from H. B. Akins et al. (2024) along with some other recent literature, divided into two groups: confirmed BL AGNs (Y. Harikane et al. 2023; R. L. Larson et al. 2023; R. Maiolino et al. 2024a; H. Übler et al. 2023; A. Bogdan et al. 2024; R. Maiolino et al. 2024b; E. Parlanti et al. 2024; H. Übler et al. 2024) and red AGNs (V. Kokorev et al. 2023; L. J. Furtak et al. 2024; J. E. Greene et al. 2024; J. Matthee et al. 2024). Assuming an Eddington ratio = 1, we show what L_{Bol} would correspond to in $\log_{10}(M_{BH}/M_\odot) = 6–8$ (horizontal dashed lines).

code models LRDs with high dust attenuation, as also found in H. B. Akins et al. (2024). In this fit, the AGN component contributes significantly to both the UV and optical portions of the spectrum. This once again highlights the challenges of SED fitting for such sources, as also demonstrated in a similar case at comparable redshift by P. Rinaldi et al. (2025). A more detailed analysis of these extreme sources, adopting different SED fitting codes, will be presented in a forthcoming study (P. Rinaldi et al. 2025, in preparation).

We also estimated the bolometric luminosity (L_{Bol}) for our photometrically selected LRDs. We computed L_{Bol} from the intrinsic best-fit SED (i.e., before any dust attenuation) using the monochromatic luminosity at 5100 Å and applying a bolometric correction of 9 (G. T. Richards et al. 2006). In the right panel of Figure 5, we show our sample of LRDs along with recent literature results (Y. Harikane et al. 2023; R. L. Larson et al. 2023; R. Maiolino et al. 2024a, 2024b; H. Übler et al. 2023, 2024; H. B. Akins et al. 2024; A. Bogdan et al. 2024; L. J. Furtak et al. 2024; J. E. Greene et al. 2024; V. Kokorev et al. 2024a; J. Matthee et al. 2024; E. Parlanti et al. 2024). We find that our sample agrees well with the region of parameter space covered by the large LRD sample presented in H. B. Akins et al. (2024), with a handful of sources reaching L_{Bol} of up to $\approx 10^{47}$ erg s^{-1}.

5. To Be an AGN or Not to Be, That Is the Question: Insights from NIRSpec

Some LRDs show broadening of the Balmer lines, suggesting that they host AGNs (e.g., J. E. Greene et al. 2024). To explore
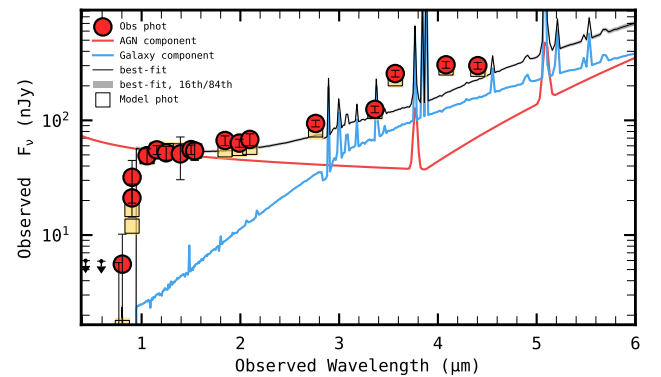
Figure 6. BAGPIPES fit for JADES-GN+189.1520+62.2596 at $z_{spec} = 6.759$. This object is also observed with NIRSpec medium-resolution gratings, which reveal broad components in both Hβ and Hα (Figure 7). The plot displays the best-fit galaxy and AGN templates from BAGPIPES. This galaxy is part of the subsample exhibiting complex UV morphology (see Figure 10). The BAGPIPES fit favors a galaxy template with high stellar mass and significant dust attenuation, consistent with findings from I. Labbé et al. (2023b) and H. B. Akins et al. (2024), further illustrating the challenges involved in modeling the SEDs of such sources as also reported in P. Rinaldi et al. (2025).

their properties, we follow the approach outlined in V. Kokorev et al. (2024a) to estimate the black hole mass (M_{BH}) under the assumption that our photometrically selected LRDs are dominated by AGNs. In general, a secure determination of M_{BH} is not feasible; however, under this assumption, we can derive an estimate. In the recent literature, the Eddington rate (λ_{Edd}) for confirmed AGNs in LRDs has been found to range

between 10% and 40% (e.g., V. Kokorev et al. 2023; L. J. Furtak et al. 2024; J. E. Greene et al. 2024).

Following the approach outlined in V. Kokorev et al. (2024a), we place a lower limit on the M_{BH} by assuming that our AGN candidates accrete at the Eddington limit, i.e., $L_{bol} \approx L_{Edd}$ (where L_{Edd} is directly proportional to M_{BH}). Under this assumption, the black hole mass is given by $M_{BH} = L_{bol}/(1.26 \times 10^{38} \text{ erg s}^{-1}) \, M_{\odot}$, where the constant comes from the canonical expression for the Eddington luminosity (e.g., G. B. Rybicki & A. P. Lightman 1979; B. M. Peterson 1997). Applying this conversion to our dust-corrected L_{bol} values yields a median $\log_{10}(M_{BH}/M_{\odot}) \approx 7.40^{+0.30}_{-0.50}$ (16th and 84th percentiles). If a significant fraction of the luminosity is derived from star formation, then this lower limit is overestimated. Using the scaling relation of J. E. Greene et al. (2020) from the estimated median $M_{\star}$ yields an estimate an order of magnitude smaller.

These values are all consistent with the recently discovered population of red and compact sources (e.g., H. B. Akins et al. 2024; V. Kokorev et al. 2024a) and similar to the black hole masses in more traditional AGNs at similar redshift (Y. Harikane et al. 2023; R. Maiolino et al. 2024a). That is, it is plausible that AGNs play an important role in any of our LRDs, including those without spectroscopic evidence for AGNs.

Among our 99 photometrically selected LRDs in the GOODS fields, 15 have NIRSpec spectra, obtained with both the prism and the medium-resolution grating (A. J. Bunker et al. 2024; F. D'Eugenio et al. 2025), including six from our fiducial sample with sufficiently high SNR for morphological analysis. Therefore, we explored whether these sources exhibit spectral signatures that could indicate the presence of AGNs. To do so, we made use of a modified version of the MSAEXP line-fitting algorithm (G. Brammer 2023), which allowed us to measure line fluxes, uncertainties, and observed equivalent widths for both the prism and gratings (V. Kokorev et al. 2025, in preparation). We also implemented a custom routine into this code to fit individual (narrow and/or broad) emission lines, deblend them when necessary, and validate the results against MSAEXP. We then excluded one source from our analysis since the quality of its spectra (both prism and medium-resolution grating) prevented us from making a proper estimation of any line fluxes. Finally, our findings were cross-matched with the official JADES line emission catalog, showing excellent agreement within the error bars.

Within our subsample of LRDs with NIRSpec spectra, we find that six (40% of the spectroscopic sample) exhibit significant broadening in the Hα emission line (either from prism or grating), with the FWHM ranging from approximately 1200–2900 km s^{-1}, as shown in Figure 7, with four of them already presented in previous works (R. Maiolino et al. 2024a; A. J. Bunker et al. 2024). Notably, one of these LRDs also shows broadening in the Hβ line (observed with the medium-resolution grating), having FWHM $\approx$2000 $\pm$ 500 km s^{-1}. We caution the reader that the low resolution of PRISM may lead to significant instrumental broadening (e.g., J. E. Greene et al. 2024). Nevertheless, some sources relying solely on PRISM data, such as GS 197348, have already been analyzed in previous studies (e.g., A. J. Bunker et al. 2023). Three of the LRDs that show broad Hα fall into our fiducial sample for morphological analysis. Unfortunately, the other three LRDs with broad Hα lack sufficient SNR in the NIRCam

SW bands (even when stacking the NIRCam SW bands), thus preventing further study of their morphology. Interestingly, one of them, with SNR $\approx$4–6 in the NIRCam SW channel (in the central region only), shows a faint component to the NW in F090W and F115W, which however is too faint to be observed in the stacked NIRCam SW image (F090W, F115W, F150W, F182M, F200W, and F210M).

To investigate further whether the selected LRDs with NIRSpec data could be classified as AGNs, we made use of two diagnostic plots based on the following emission lines: [O II] $\lambda\lambda$3727, 3728, [Ne III] λ3870, Hβ λ4861, and [O III] λ5007. In particular, we explored the following ratios: [O III] λ5007/Hβ versus [Ne III] λ3870/[O II] $\lambda\lambda$3727 (commonly referred to as the "OHNO" diagram) and [O III] λ4363/Hγ versus [O III] λ5007/[O II] $\lambda\lambda$3727. Below, we present our results.

The OHNO diagram. In the left panel of Figure 8, we analyze our LRD sample by employing the "OHNO" diagram (L. Trouille et al. 2011; G. R. Zeimann et al. 2015; B. E. Backhaus et al. 2022, 2023; N. J. Cleri et al. 2023; J. R. Trump et al. 2023; L. M. Feuillet et al. 2024), as the [Ne III] λ3870/[O II] $\lambda\lambda$3727, 3728 ratio has proven to be a robust ionization diagnostic for high-redshift galaxies (e.g., B. E. Backhaus et al. 2022, 2023, 2024). This diagnostic is particularly effective because [Ne III] λ3870 and [O II] $\lambda\lambda$3727, 3728 have similar ionization energy, and their being very close in wavelength minimizes the effects of dust attenuation. In particular, it has been shown that employing this ratio can effectively help in distinguishing between star-forming galaxies (SFGs) and AGNs (see G. R. Zeimann et al. 2015; B. E. Backhaus et al. 2022, 2023, 2024). While this diagram is primarily sensitive to ionization, it also shows a dependence on metallicity (e.g., R. Tripodi et al. 2024). Therefore, we caution the reader that low-metallicity galaxies may introduce contamination, as already discussed in J. Scholtz et al. (2025).

On average, our photometrically selected LRDs exhibit $\log_{10}([\text{O III}]_{5007}/\text{H}\beta) \gtrsim 0.5$ (median value of 0.71 $\pm$ 0.03), with the exception of one source that suffers from poor data quality in both prism and medium-resolution modes. Overall, the members of our sample show a consistently high [Ne III] λ3870/[O II] $\lambda\lambda$3727 ratio compared to the average SFG population. Interestingly, our sample occupies the same region of other LRDs recently studied in the literature (e.g., M. Killi et al. 2024; D. D. Kocevski et al. 2023b; V. Kokorev et al. 2023; R. L. Larson et al. 2023) and, in general, the region occupied by selected BL and/or narrow-line AGNs (e.g., J. Scholtz et al. 2025; H. Übler et al. 2024). The gray area represents the sample of SFGs and AGNs selected from the Sloan Digital Sky Survey at $z \approx 0$ from D. G. York et al. (2000).

The [O III] λ4363/Hγ versus [O III] λ5007/[O II] λ3727 diagram. In the right panel of Figure 8, we show another diagnostic diagram to investigate the nature of our photometrically selected LRDs: the [O III] λ4363/Hγ versus [O III] λ5007/[O II] λ3727 diagram. This diagram has been recently presented in G. Mazzolari et al. (2024) and, like the OHNO diagram, offers the advantage of using line ratios that lie very close to each other in wavelength, therefore reducing the effects of dust reddening.

Recent studies have demonstrated that some high-redshift galaxies ($z \gtrsim 8$) exhibit anomalously high [O III] λ4363 emission, potentially suggesting the presence of an AGN (e.g., J. Brinchmann 2023). Intriguingly, this trend has been further
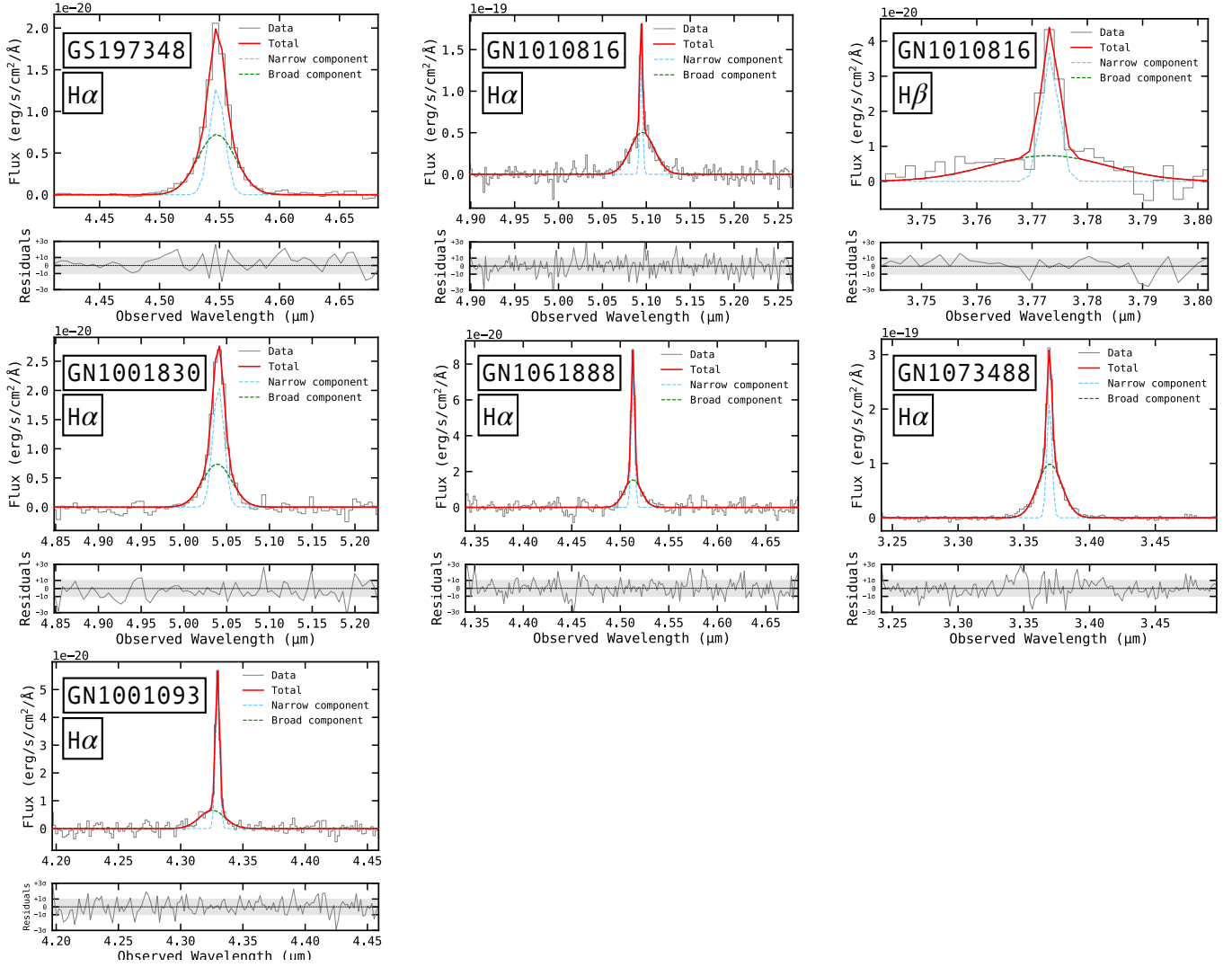
Figure 7. The six LRDs that show broadening in their Hα from NIRSpec data (NIRCam IDs, see Table 1): GS 197348, GN 1010816, GN 1001830, GN 1061888, GN 1073488, and GN 1001093. In particular, GN 1010816 (red frame) shows also broadening in its Hβ. Some of these objects are already reported in previous works, namely GS 197348, GN 1010816, GN 1001093, and GN 1061888 (R. Maiolino et al. 2024a; A. J. Bunker et al. 2024).

confirmed by H. Übler et al. (2024), who suggested that a strong [O III] λ4363/Hγ ratio could actually result from higher interstellar medium (ISM) temperatures driven by AGN activity and thus point to the presence of an AGN. We remind the reader that, while this diagnostic is similar to the OHNO diagram, the separation between AGNs and SFGs in this case is primarily driven by differences in the gas temperature.

As demonstrated by G. Mazzolari et al. (2024), normal SFGs (and their local analogs) tend to populate a well-defined region in this diagram, specifically the lower-right portion of the plot. In contrast, the AGN population spans a broader area, including the upper-left region. In particular, following the discussion presented by G. Mazzolari et al. (2024), who tested models computed by J. Gutkin et al. (2016), A. Feltre et al. (2016), and K. Nakajima & R. Maiolino (2022), that area cannot be populated by any SFG model (see their Figure 1b for a more comprehensive view).

The strength of the [O III] λ4363 emission line, which is produced through collisional excitation from high-energy levels, lies in its ability to provide key information about the gas temperature when compared to the Hγ intensity (e.g., R. L. Sanders et al. 2016). This ratio can also offer insights

into the metallicity of the ISM and the ionization parameter (e.g, T. Gburek et al. 2019). The primary difference between SFGs and AGNs lies in the source of their ionizing radiation—young star clusters in the former and emission from the accretion disk in the latter, resulting in significantly more powerful ionizing radiation in the case of AGNs. This leads to higher electron temperatures, which, in turn, increase the [O III] λ4363 emission and the [O III] λ4363/Hγ ratio for a given ionization parameter (i.e., the ratio of the number density of incident ionizing photons to the number density of hydrogen atoms).

We observe that six sources lie above the separation line provided by G. Mazzolari et al. (2024), and more broadly, they overlap with the sample of AGNs (and some selected LRDs) identified in recent studies (e.g., M. Curti et al. 2023; V. Kokorev et al. 2023; K. Nakajima et al. 2023; J. Scholtz et al. 2025; H. Übler et al. 2023; I. Juodžbalis et al. 2024b; H. Übler et al. 2024). Notably, one source is placed significantly above the separation line, although we caution the reader that the spectral region of [O III] λ4363/Hγ has a low SNR for this source. Interestingly, this source does not exhibit any clear signature of broad components in its Balmer
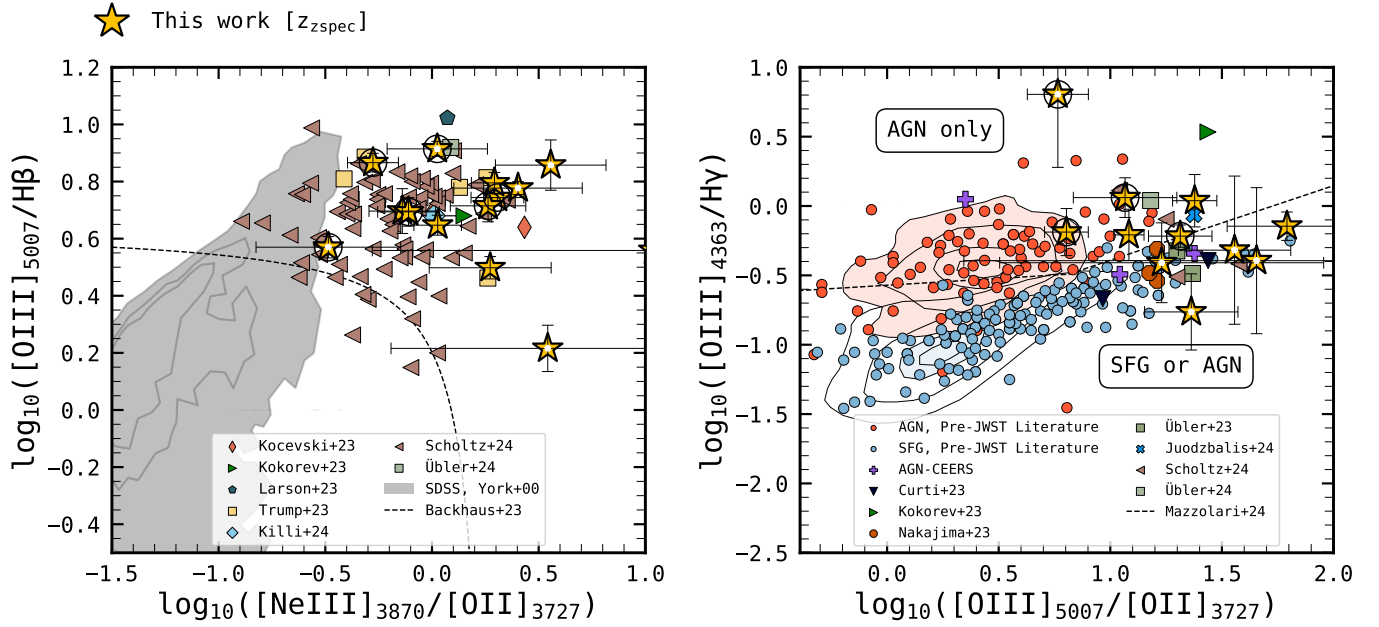
Figure 8. Left panel: we show the "OHNO" diagram. We present our sources as gold stars along with the recent literature from D. D. Kocevski et al. (2023b), V. Kokorev et al. (2023), R. L. Larson et al. (2023), J. R. Trump et al. (2023), M. Killi et al. (2024), J. Scholtz et al. (2025), and H. Übler et al. (2024). For comparison, we also show the Sloan Digital Sky Survey sample (SFGs and AGNs) at low z from D. G. York et al. (2000). The demarcation line comes from B. E. Backhaus et al. (2023). Right panel: we replicate the panel shown in G. Mazzolari et al. (2024). Our sources are shown as gold stars along with some recent literature: M. Curti et al. (2023), V. Kokorev et al. (2023), K. Nakajima et al. (2023), H. Übler et al. (2023), I. Juodžbalis et al. (2024b), J. Scholtz et al. (2025), and H. Übler et al. (2024). We also show the demarcation line from G. Mazzolari et al. (2024). Pre-JWST literature for AGNs and SFGs is shown as well (e.g., Y. I. Izotov et al. 2007; R. Amorín et al. 2015). The stars marked with black circles are the objects with enough SNR for morphological studies. The sources marked with a white dot are the ones with SNR $\lesssim 2$ for one of the two line ratios involved in these diagnostics.

lines, but shows both [N II] $\lambda6548$ and [N II] $\lambda6583$ (detected with an SNR of approximately 4–6 in the medium-resolution grating). By inspecting its [N II]/Hα ratio, we find that this source would lie precisely on the separation line between AGNs and SFGs in the classic "Baldwin, Phillips, and Terlevich" diagram (J. A. Baldwin et al. 1981).

More generally, our sample of photometrically selected LRDs is well constrained within a defined region of the parameter space, which overlaps with the area predominantly populated by recently discovered AGNs using JWST. However, we note that this region, just below the demarcation line, also includes a subset of SFGs (pale blue circles; e.g., Y. I. Izotov et al. 2007; R. Amorín et al. 2015; M. Curti et al. 2023; K. Nakajima et al. 2023; J. Scholtz et al. 2025).

Altogether, these two panels highlight the diversity of our LRD sample, ranging from pure AGNs to composite galaxies, underscoring their complex nature as a mix of different ionizing sources, as also suggested by previous studies (e.g., P. G. Pérez-González et al. 2024). The consistency of our results, with our objects occupying a region of parameter space shared by AGN-dominated systems and SFGs, further supports their mixed nature. This suggests that AGN activity might significantly influence the properties of this subset of photometrically selected LRDs, though the extent of this influence remains unclear and warrants deeper spectroscopic investigation. We also note that these diagnostic plots are subject to uncertainties, including potential redshift dependencies (see discussion in P. Rinaldi et al. 2025, Section 3.4.2), which must be considered when interpreting the nature of these sources. In Table 3, we report the line fluxes estimated for each source.

Finally, we computed M_{BH} for the six sources that show broadening in Hα and compared the estimated quantities with the recent literature. To estimate M_{BH}, we followed the approach presented in A. E. Reines et al. (2013), for which M_{BH} can be estimated as follows:

$$\log_{10}\left(\frac{M_{BH}}{M_\odot}\right) = \alpha + \log_{10}(\varepsilon) + \beta \log_{10}\left(\frac{L_{H\alpha,broad}}{1 \times 10^{42} \text{ erg s}^{-1}}\right)$$
$$+ \gamma \log_{10}\left(\frac{FWHM_{broad}}{1 \times 10^3 \text{ km s}^{-1}}\right),$$

$$(1)$$

where $\alpha = 6.57$, $\beta = 0.47$, and $\gamma = 2.06$.

The results are shown in Figure 9. Overall, our findings align with recent studies of selected LRDs analyzed using spectroscopic data (e.g., V. Kokorev et al. 2023). They also tend to validate our rough estimates made previously.

6. Morphology of LRDs with Broad Hα

Among the LRD candidates with NIRSpec spectra, three show a sufficiently high SNR and extent for morphological analysis, as well as broad Hα (Figure 10). Given the potential for both AGN and star-forming activity that these features imply (in combination with the results of the various spectral line-ratio diagnostics discussed in the previous section), we consider that their highly disturbed appearance may be associated with one or both of these processes, and potentially result from merging activity. As shown in Figure 10, GN 1010816 is detected with multiple distinct regions of emission (four, according to its I statistic measure), at least two of which are of comparable intensity and size, and with a total spatial extent measured to have significant asymmetry. Given the sampling of rest-UV emission in the stacked NIRCam SW channel images used for morphological characterization, this
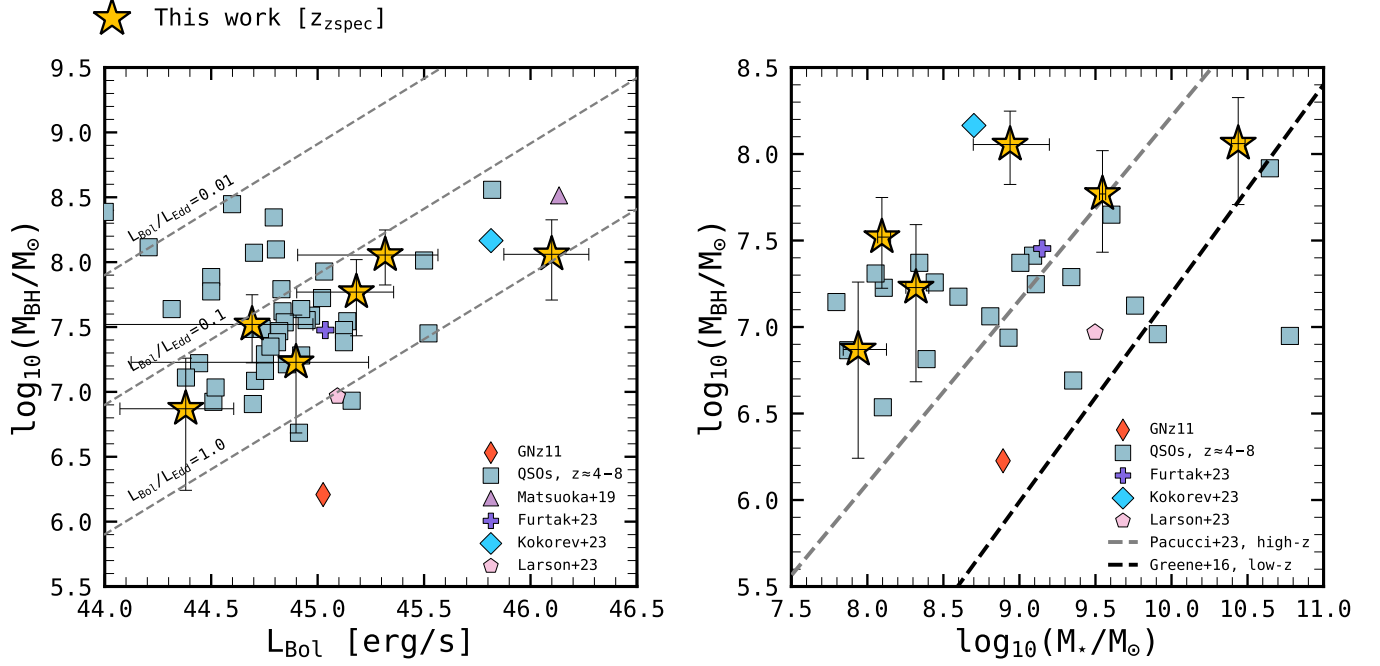
Figure 9. Left panel: the derived black hole mass ($M_{\rm BH}$) as a function of bolometric luminosity ($L_{\rm Bol}$), in comparison with recent findings in the literature (e.g., GNz11, CEERS_1019, and triply lensed quasars, among others; Y. Matsuoka et al. 2019; L. J. Furtak et al. 2023; Y. Harikane et al. 2023; D. D. Kocevski et al. 2023b; V. Kokorev et al. 2023; R. L. Larson et al. 2023; R. Maiolino et al. 2024a, 2024b; J. Matthee et al. 2024). The dashed lines represent bolometric luminosities corresponding to Eddington ratios of $L_{\rm Bol}/L_{\rm Edd} = 0.01$, 0.1, and 1.0. Right panel: the black-hole-to-stellar mass relation is presented, with the bold black dashed line indicating the best fit to $z \approx 0$ AGN samples (J. E. Greene et al. 2016). The trend at higher redshifts is based on the recent analysis by F. Pacucci et al. (2023). Color codes and markers are the same as those in the left panel.

Table 3
Emission Line Measurements for LRDs with NIRSpec Data

NIRCam ID	[O III] $\lambda5007$	Hβ	[Ne III] $\lambda3870$	[O II] $\lambda3727$	Hγ	[O III] $\lambda4363$
197348	454.93 ± 9.19	82.06 ± 1.71	33.63 ± 2.19	16.60 ± 4.60	⋯	⋯
110739	744.32 ± 11.30	167.73 ± 13.23	65.33 ± 13.37	61.43 ± 9.53	82.37 ± 15.76	51.02 ± 19.41
206858	594.88 ± 27.17	160.08 ± 11.82	33.40 ± 23.90	102.21 ± 31.84	$2.84 \pm 1.86^{*}$	$18.15 \pm 18.53^{*}$
210600	723.67 ± 41.44	98.51 ± 4.85	34.09 ± 6.94	64.45 ± 11.85	⋯	⋯
1010816	1200.75 ± 22.27	146.24 ± 8.46	109.16 ± 9.90	$103.10 \pm 55.01^{*}$	59.46 ± 11.19	68.35 ± 18.46
1001093	226.02 ± 8.77	62.44 ± 11.59	54.70 ± 17.70	$4.99 \pm 15.09^{*}$	$17.22 \pm 9.77^{*}$	$6.95 \pm 7.45^{*}$
1001830	531.57 ± 14.61	73.80 ± 14.83	53.12 ± 7.66	14.75 ± 8.54	21.89 ± 8.22	$10.52 \pm 12.32^{*}$
1004685	84.27 ± 7.88	51.27 ± 8.29	17.30 ± 4.76	$4.96 \pm 8.28^{*}$	19.58 ± 5.00	$7.63 \pm 4.67^{*}$
1013041	918.91 ± 18.09	153.56 ± 7.42	37.59 ± 11.85	$14.85 \pm 9.16^{*}$	67.78 ± 8.45	48.49 ± 9.70
1032447	1231.22 ± 20.99	197.28 ± 16.30	101.14 ± 10.06	51.55 ± 11.74	55.17 ± 18.15	60.27 ± 17.16
1034762	298.76 ± 11.13	60.08 ± 10.63	35.04 ± 7.15	48.28 ± 14.29	38.36 ± 14.20	⋯
1061888	283.32 ± 7.26	89.99 ± 7.77	23.03 ± 10.33	12.29 ± 5.91	109.07 ± 17.45	$18.80 \pm 11.50^{*}$
1073488	1161.28 ± 14.23	223.88 ± 28.73	103.35 ± 25.05	56.44 ± 18.47	145.62 ± 12.02	88.34 ± 14.60
1079572	680.03 ± 18.51	137.64 ± 15.40	83.01 ± 20.43	106.93 ± 23.94	109.61 ± 15.76	71.11 ± 25.83

Note. Emission line measurements are given as the flux $\pm$ error in units of 10^{-20} erg s cm^2. Sources with * have SNR < 2 for the respective line.

example could indicate multiple merging galaxies, triggering bursts of star formation in the form of UV clumps (e.g., Y. Guo et al. 2015), and/or one or two unobscured AGNs. It is also possible that the multiple components of emission do not represent distinct nuclei in the act of merging, but a single galaxy (possibly in the postmerger phase) with a surrounding clumpy structure from merger- and/or AGN-triggered star formation, and/or clumpy accretion onto an AGN (e.g., C. DeGraf et al. 2017).

The other two LRDs with broad Hα line emission appear as single sources with a highly asymmetric spatial footprint, as determined through both human and computer vision. GN 1073488 appears distinctly bright and pointlike and is

embedded in an asymmetric diffuse structure. GS 197348, on the other hand, appears elongated, with a relatively long, narrow, and faint emission structure appearing to "shoot off" from one of its sides. This faint extended feature is notably missed by the MID statistics, but is caught by the A$_S$ algorithm, which was explicitly designed to detect such faint edge features. If this feature is real and associated with the LRD—which it appears to be based on its presence in all the NIRCam SW filters considered—it could potentially be a manifestation of AGN feedback, e.g., the UV emission that has been found to spatially coincide with AGN radio jets (e.g., K. Rubinur et al. 2024).
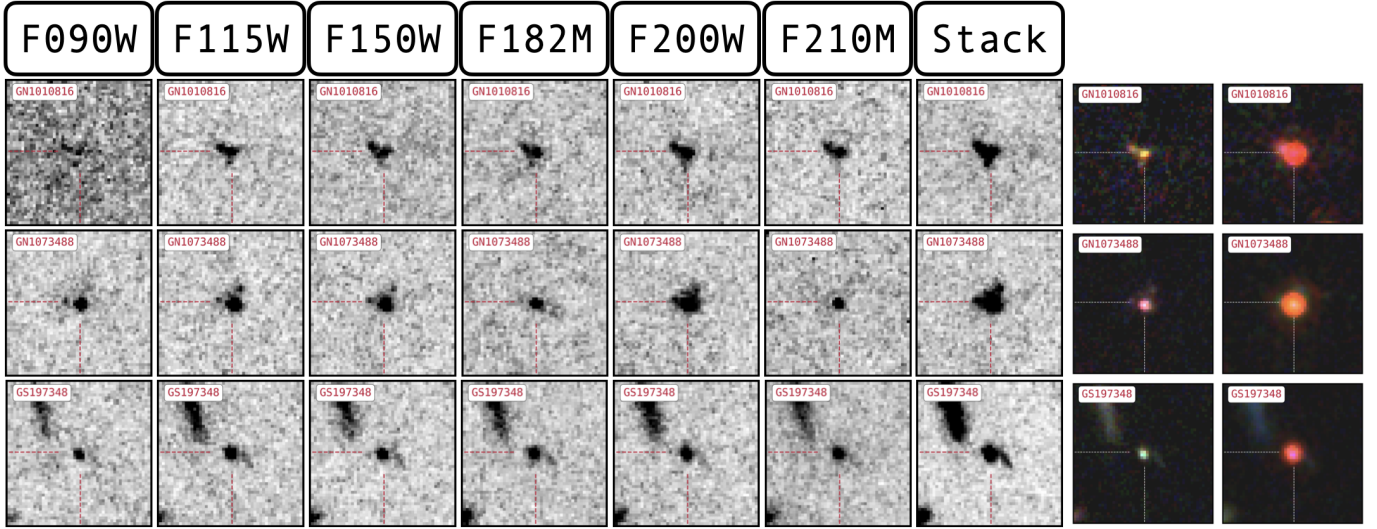
Figure 10. The LRDs in our sample with NIRSpec spectra that show broad Hα line emission (and with sufficient SNR for morphological characterization), possibly indicating the presence of an AGN. The postage stamps (1″.5 × 1″.5) are from the NIRCam SW channel (F090W, F115W, F150W, F182M, F200W, and F210M). For visual comparison, we also show the RGB postage stamps considering the SW bands only and the "classic" RGB (i.e., F090W, F277W, and F444W).

7. Summary and Discussion

In this study, we analyzed a sample of 99 photometrically identified LRDs in the GOODS fields, selected using color and compactness criteria (Figures 1 and 2; e.g., I. Labbé et al. 2023b).

We examined the rest-wavelength UV morphology of these LRDs by analyzing ultradeep NIRCam SW images using the STATMORPH software. Out of 99 photometrically selected LRDs, 30% show extended structure and also sufficient SNR in these bands to allow for a meaningful morphological analysis. The remaining 70% are strongly dominated by sources $\lesssim 400$ pc in diameter and lack extended components even in stacked SW-band images. We found that all these objects exhibit $A_S > 0.2$, with a median value of ≈ 0.5, suggesting that these sources are generally highly spatially disturbed and likely to be undergoing mergers or interactions. Such elevated A_S values align with recent findings (e.g., N. Bonaventura et al. 2025), which suggest that galaxies with $A_S > 0.2$ are frequently linked to ongoing or recent merger activity (Figures 3 and 4).

While most studies consider the rest-optical emission of galaxies in diagnosing merger morphologies, we have analyzed the rest-UV morphology of LRDs at $z \approx 4$–8 imaged in the NIRCam SW bands. The expectation from the results of V. A. Mager et al. (2018) is that the UV asymmetry of merging/peculiar galaxies will be consistent with, or appear more pronounced than, that measured in the rest-optical, for all galaxy types: these authors observe a significant increase in the clumpiness of all galaxy types at shorter wavelengths. Furthermore, more recent studies on high-z galaxy morphology have shown that, in general, galaxies do not exhibit dramatic changes when transitioning from UV to optical light. For instance, T. Treu et al. (2023) studied a sample of Lyman-break galaxies during the epoch of reionization and found that, within the uncertainties and scatter, the classic morphological indices (G, M_{20}, A, etc.) remain relatively consistent across different wavelengths. That is, the measures of galaxy morphology in our study should reflect those expected from the rest-optical emission. However, a caveat to consider in the rest-UV is that, without knowledge of the quantity, distribution, optical depth, and covering fraction of the dust present in a galaxy, the extent to which it may be affecting the observed rest-UV morphology cannot be constrained. While it is possible that the presence of severely attenuating dust could contribute to a clumpy UV morphology by blocking from view all but the brightest UV emission regions, it is unlikely that the 30 star-forming LRDs included in our morphological analysis appear with such irregular and extended features purely as a result of this effect.

The disturbed LRD morphology we observe could be driven by gravitational interactions that channel gas toward the central regions, potentially fueling both star formation and black hole growth, and finally leading to an AGN phase. However, quite surprisingly, preliminary analysis of the stacked X-ray emission of the LRDs using the deepest available Chandra ACIS-I imaging coverage, from the CDFS 7Ms survey, shows no detection; this mirrors the findings of M. Yue et al. (2024), who were equally baffled by the nondetection of stacked X-ray emission of their LRD sample. Gas accretion onto an AGN should exhibit significant X-ray luminosity, as well as the shock-heated gas of a major, gas-rich galaxy merger (e.g., T. J. Cox et al. 2006 and references therein). Therefore, it is conceivable that, in X-ray-undetected LRDs, a dynamical or other physical process is preventing the angular momentum of the gas in the system from dropping low enough to funnel onto the nucleus, causing a delay to the infall of tidal material and the consequent detectable X-ray emission. For instance, several galaxy merger simulations suggest that the higher gas turbulence and velocity dispersion observed in high-redshift galaxies in comparison to their lower-redshift counterparts inhibit the propagation of gas inflows toward the center of the system, possibly resulting in suppressed AGN activity in gaseous, high-redshift galaxies (see E. A. Shah et al. 2020 and references therein). In any case, low X-ray luminosity has been found for a variety of other high-redshift AGNs (J. Lyu et al. 2024; R. Maiolino et al. 2025), so the puzzle is not confined to LRDs.

To put the morphology results in context, we employed BAGPIPES to analyze the properties of all 99 LRDs and found

that, on average, the sources exhibit $A_V \approx 2.74^{+0.55}_{-0.71}$ mag (16th and 84th percentiles) when AGN models are included, and $A_V \approx 1.16^{+0.11}_{-0.21}$ mag (16th and 84th percentiles) when using stellar models only. The average stellar mass is $\log_{10}(M_\star/M_\odot) \approx 9.67^{+0.17}_{-0.27}$ (16th and 84th percentiles), or $\log_{10}(M_\star/M_\odot) = 9.07^{+0.11}_{-0.08}$ (16th and 84th percentiles) when stellar models only are considered. To first order, the difference in $M_\star$ is a reflection of different dust extinctions. We also estimated their (dust-corrected) $L_{\rm Bol}$ from their best-fit spectra (assuming a correction factor of ≈ 9; G. T. Richards et al. 2006). By making the assumption that all these selected LRDs host AGNs and adopting an Eddington ratio of 1, we derived lower limits for their $M_{\rm BH}$, with a median value of $\log_{10}(M_{\rm BH}/M_\odot) \approx 7.40^{+0.30}_{-0.50}$ (16th and 84th percentiles), or an order of magnitude smaller if we estimated black hole masses from the usual relation with the $M_\star$ (J. E. Greene et al. 2020). These results are also consistent with those reported for the recently discovered population of red and compact sources (e.g., H. B. Akins et al. 2024; V. Kokorev et al. 2024a), i.e., our sample is typical of the general class.

Among our sample of LRDs, 15 have NIRSpec spectra, which have been explored to investigate whether they host an AGN. We employed three different diagnostic diagrams to evaluate the state of their ISM. We found a variety of behavior, ranging from those classified as pure AGNs to those showing a mixed nature (i.e., classified as composite galaxies), indicating their complex nature (Figure 8). Interestingly, six of them exhibit broadening in their Hα lines, with one also showing broadening in Hβ. The remaining 60% show no clear signs of AGN presence (i.e., no broadening in their Balmer lines); nonetheless, the diagnostic plots employed in this study hint at either AGN activity or a mixed nature for these sources, suggesting that deeper spectroscopic data are needed to further investigate their nature. For those showing broad Hα, we estimated their $M_{\rm BH}$ from the broad Hα component (A. E. Reines et al. 2013) and found that our results are consistent with recent findings about LRDs (Figure 9; e.g., L. J. Furtak et al. 2023; V. Kokorev et al. 2023; R. L. Larson et al. 2023).

A significant portion of our LRD sample exhibits disturbed UV morphology, with some objects clearly observed in a merger state (Figure 10). Two sources with NIRSpec data show very high $M_\star$ and highly disturbed UV morphology (Figure 5). The most reliably modeled of these sources shows a very high $M_\star$ ($\log_{10}(M_\star/M_\odot) = 10.62^{+0.05}_{-0.05}$) at $z_{\rm spec} = 6.759$.

The mechanisms that trigger rapid gas accretion onto supermassive black holes (SMBHs) remain still unclear, which directly ties into the nature of the LRDs in our sample. A compelling theoretical hypothesis is that galaxy mergers and interactions drive AGN activity by funneling gas into the central regions of galaxies, thereby fueling the SMBH (e.g., J. M. Gabor et al. 2016; K. A. Blumenthal & J. E. Barnes 2018), also recently supported by Q. Duan et al. (2025). However, observational evidence remains inconclusive, with several studies finding no definitive correlation (e.g., C. Villforth et al. 2014; T. Hewlett et al. 2017; S. L. Ellison et al. 2019; D. D. Kocevski et al. 2023a; J. C. S. Pierce et al. 2023). Given that our morphological analysis revealed significant asymmetries and signs of disturbance in a substantial fraction of our LRDs, it is plausible that interactions might play a substantial role in triggering AGNs in these systems (although we do not have a control sample to put this on a more quantitative basis). This would be an important, although perhaps not unexpected, difference from the situation at lower redshift. Further spectroscopic and morphological studies, particularly those utilizing deep NIRSpec integral field unit data, will be essential in unveiling the true nature of LRDs and exploring the connection between their disturbed UV morphologies and potential AGN activity.

Data Availability

The JADES and HLF data used in this research are available from the Mikulski Archive for Space Telescopes (MAST) at the Space Telescope Science Institute (G. Illingworth 2015; M. Rieke et al. 2023).

Facilities: HST, JWST.

Software: ASTROPY (Astropy Collaboration et al. 2022), BAGPIPES (A. C. Carnall et al. 2019), MSAEXP (G. Brammer 2023), NUMPY (C. R. Harris et al. 2020), PANDAS (The pandas development team 2024), PHOTUTILS (L. Bradley et al. 2016), TOPCAT (M. Taylor 2022).

Appendix A

Here we present the mathematical formalisms underpinning the MID and shape asymmetry A_S morphology indicators chosen to characterize the LRDs of the present study. We utilized the STATMORPH code for the morphology analysis, which reads a galaxy image and its associated weight map (the 1σ error image, also known as the "sigma image" in Galfit and similar image analyses) to examine both the brightness and spatial distribution of its pixel values. It then calculates various galaxy morphology metrics, including the following nonparametric measures of galaxy structure: asymmetry (A), clumpiness (S), concentration index (C), Gini index (G), and moment of light (M_{20}) (J. M. Lotz et al. 2004, K. L.-K. Wu 1999, M. A. Bershady et al. 2000, C. J. Conselice et al. 2000). STATMORPH computes the MID and A_S statistics as detailed below, with slight modifications to their original definitions as presented in P. E. Freeman et al. (2013) and M. M. Pawlik et al. (2016), respectively (V. Rodriguez-Gomez et al. 2019).

Appendix B
MID Statistics

The STATMORPH software calculates the nonparametric MID statistics according to their original definitions in P. E. Freeman et al. (2013), except for the multimode (M) statistic, for which a modified version defined in M. A. Peth et al. (2016) is adopted. The algorithm defining the M statistic locates all noncontiguous groups of image pixels that lie above a given intensity threshold, q, sorts them by pixel area, then computes the area ratio of the second-largest group ($A_{q,2}$) to the first ($A_{q,1}$); this process is then repeated for a number of intensity thresholds. M represents the maximum area ratio resulting from all the trials:

$$M = \max_q(A_{q,2}/A_{q,1}). \tag{B1}$$

As such, M values approaching 1 are likely to indicate a double nucleus, while values close to zero should be interpreted as a single source (i.e., where the nonzero detection of a relatively small, secondary pixel group is likely to be noise).

The intensity (I) statistic serves as a complement to M in that it computes the intensity ratio of the two brightest source regions in the galaxy image. It does so by first locating all the distinct intensity maxima in a smoothed image of the galaxy emission, identifying and summing the intensities of the group of pixels belonging to each intensity peak, and then calculating the ratio of the summed intensity of the second-brightest pixel group (I_2) to the first (I_1):

$$I = I_2/I_1. \tag{B2}$$

It should be noted that, due to the different ways in which the M and I statistics are calculated, they may not simultaneously detect multiple sources/components of emission in a given galaxy image. In other words, M is a function of the spatial footprint of distinct regions in the galaxy emission, while I considers their relative intensities. However, this can be a useful difference in cases of relatively faint emission components/ sources and/or low resolution, where one of the statistics can provide an independent, compensating measure where the other statistic fails to detect multiple image components (or confirms the finding of the other where both agree). Such a scenario could occur where M detects multiple distinct regions of emission within the galaxy image, but I does not resolve more than one local intensity maximum. There can also be a case where the I statistic locates a relatively small but bright secondary region of emission that leads to a disproportionately small value of M.

The deviation (D) statistic provides a measure of the normalized distance between the centroid of the total extent of the galaxy emission as identified in the segmentation map and its brightest local intensity maximum. This statistic is therefore useful in identifying irregular/peculiar galaxy shapes—e.g., late-stage or postcoalescent mergers, or active sources experiencing significant spatial disruption from star-forming and/or AGN processes—given the expectation that symmetric and ordered morphologies such as spheroids and disks would show a D value close to zero. It is calculated according to the following formula, where the image centroid is represented by (x_c, y_c), the brightest peak resulting from the I statistic calculation is (x_{I_1}, y_{I_1}), and n_{seg} is the number of pixels in the segmentation map:

$$D = \sqrt{\pi/n_{seg}} \sqrt{(x_c - x_{I_1})^2 + (y_c - y_{I_1})^2}. \tag{B3}$$

Appendix C
Shape Asymmetry (A_S)

The A_S parameter is calculated in exactly the same way as the classic A parameter, except that it is performed on the binary detection mask as opposed to the corresponding image containing the source emission (M. M. Pawlik et al. 2016). As such, A_S traces only the spatial outline of a galaxy image, while A considers asymmetries in both the pixel intensity values and their spatial locations within the emission image. Due to the assignment of equal weights to all components of the galaxy, without regard to their relative brightness, A_S is more sensitive to features with low surface brightness along the galaxy edges. The mathematical formalism is shown below, and essentially involves subtracting a 180° rotated image of the galaxy from the original image, measuring the sum of the fractional pixel intensity ($I_{i,j}$) changes due to the rotation, and then subtracting from this a measure of the average asymmetry of the background emission.

$$A = \sum_{i,j}|I_{i,j} - I_{i,j}^{180}|/\sum_{i,j}|I_{i,j}| - A_{bgr}. \tag{C1}$$

ORCID iDs

P. Rinaldi ◉ https://orcid.org/0000-0002-5104-8245
N. Bonaventura ◉ https://orcid.org/0000-0001-8470-7094
G. H. Rieke ◉ https://orcid.org/0000-0003-2303-6519
S. Alberts ◉ https://orcid.org/0000-0002-8909-8782
K. I. Caputi ◉ https://orcid.org/0000-0001-8183-1460
W. M. Baker ◉ https://orcid.org/0000-0003-0215-1104
S. Baum ◉ https://orcid.org/0000-0002-4735-8224
R. Bhatawdekar ◉ https://orcid.org/0000-0003-0883-2226
A. J. Bunker ◉ https://orcid.org/0000-0002-8651-9879
S. Carniani ◉ https://orcid.org/0000-0002-6719-380X
E. Curtis-Lake ◉ https://orcid.org/0000-0002-9551-0534
F. D'Eugenio ◉ https://orcid.org/0000-0003-2388-8172
E. Egami ◉ https://orcid.org/0000-0003-1344-9475
Z. Ji ◉ https://orcid.org/0000-0001-7673-2257
B. D. Johnson ◉ https://orcid.org/0000-0002-9280-7594
K. Hainline ◉ https://orcid.org/0000-0003-4565-8239
J. M. Helton ◉ https://orcid.org/0000-0003-4337-6211
X. Lin ◉ https://orcid.org/0000-0001-6052-4234
J. Lyu ◉ https://orcid.org/0000-0002-6221-1829
R. Maiolino ◉ https://orcid.org/0000-0002-4985-3819
P. G. Pérez-González ◉ https://orcid.org/0000-0003-4528-5639
M. Rieke ◉ https://orcid.org/0000-0002-7893-6170
B. E. Robertson ◉ https://orcid.org/0000-0002-4271-0364
I. Shivaei ◉ https://orcid.org/0000-0003-4702-7561
M. Stone ◉ https://orcid.org/0000-0002-9720-3255
Y. Sun ◉ https://orcid.org/0000-0001-6561-9443
S. Tacchella ◉ https://orcid.org/0000-0002-8224-4505
H. Übler ◉ https://orcid.org/0000-0003-4891-0794
C. C. Williams ◉ https://orcid.org/0000-0003-2919-7495
C. N. A. Willmer ◉ https://orcid.org/0000-0001-9262-9997
C. Willott ◉ https://orcid.org/0000-0002-4201-7367
J. Zhang ◉ https://orcid.org/0000-0002-1574-2045
Y. Zhu ◉ https://orcid.org/0000-0003-3307-7525

References

Akins, H. B., Casey, C. M., Lambrides, E., et al. 2024, arXiv:2406.10341
Alberts, S., Lyu, J., Shivaei, I., et al. 2024, ApJ, 976, 224
Amorín, R., Pérez-Montero, E., Contini, T., et al. 2015, A&A, 578, A105
Astropy Collaboration, Price-Whelan, A. M., Lim, P. L., et al. 2022, ApJ, 935, 167
Backhaus, B. E., Bridge, J. S., Trump, J. R., et al. 2023, ApJ, 943, 37
Backhaus, B. E., Trump, J. R., Cleri, N. J., et al. 2022, ApJ, 926, 161
Backhaus, B. E., Trump, J. R., Pirzkal, N., et al. 2024, ApJ, 962, 195
Baggen, J. F. W., van Dokkum, P., Brammer, G., et al. 2024, ApJL, 977, L13
Bagley, M. B., Pirzkal, N., Finkelstein, S. L., et al. 2024, ApJ, 965, L6
Baldwin, J. A., Phillips, M. M., & Terlevich, R. 1981, PASP, 93, 5
Barro, G., Pérez-González, P. G., & Kocevski, D. D. 2024, ApJ, 963, 128
Blumenthal, K. A., & Barnes, J. E. 2018, MNRAS, 479, 3952
Bogdan, A., Goulding, A. D., Natarajan, P., et al. 2024, NatAs, 8, 126
Bonaventura, N., Lyu, J., Rieke, G. H., et al. 2025, ApJ, 978, 74
Bouwens, R. J., Illingworth, G. D., González, V., et al. 2010, ApJ, 725, 1587
Boyett, K., Bunker, A. J., Curtis-Lake, E., et al. 2024, MNRAS, 535, 1796
Boylan-Kolchin, M. 2023, NatAs, 7, 731
Bradley, L., Sipocz, B., Robitaille, T., et al., 2016 Photutils: Photometry tools, Astrophysics Source Code Library v2.2, ascl:1609.011
Bradley, L. D., Coe, D., Brammer, G., et al. 2023, ApJ, 955, 13
Brammer, G. 2023, msaexp: NIRSpec analysis tools, v0.6.17, doi:10.5281/zenodo.7299500
Brinchmann, J. 2023, MNRAS, 525, 2087
Bruzual, G., & Charlot, S. 2003, MNRAS, 344, 1000
Bunker, A. J., Cameron, A. J., Curtis-Lake, E., et al. 2024, A&A, 690, A288
Bunker, A. J., Saxena, A., Cameron, A. J., et al. 2023, A&A, 677, A88
Buta, R. J. 2011, arXiv:1102.0550
Calzetti, D., Armus, L., Bohlin, R. C., et al. 2000, ApJ, 533, 682
Caputi, K. I., Rinaldi, P., Iani, E., et al. 2024, ApJ, 969, 159

Carnall, A. C., McLure, R. J., Dunlop, J. S., et al. 2019, MNRAS, 490, 417
Carnall, A. C., McLure, R. J., Dunlop, J. S., et al. 2023, Natur, 619, 716
Chen, C.-H., Ho, L. C., Li, R., & Zhuang, M.-Y. 2025, ApJ, 983, 60
Cleri, N. J., Olivier, G. M., Hutchison, T. A., et al. 2023, ApJ, 953, 10
Conselice, C. J., Bershady, M. A., & Gallagher, J. S. III. 2000, A&A, 354, 21
Conselice, C. J., Chapman, S. C., & Windhorst, R. A. 2003, ApJ, 596, L5
Cox, T. J., Di Matteo, T., Hernquist, L., et al. 2006, ApJ, 643, 692
Curti, M., D'Eugenio, F., Carniani, S., et al. 2023, MNRAS, 518, 425
DeGraf, C., Dekel, A., Gabor, J., & Bournaud, F. 2017, MNRAS, 466, 1462
Desprez, G., Martis, N. S., Asada, Y., et al. 2024, MNRAS, 530, 2935
D'Eugenio, F., Cameron, A. J., Scholtz, J., et al. 2025, ApJS, 277, 4
Duan, Q., Li, Q., Conselice, C. J., et al. 2025, MNRAS, 540, 774
Durodola, E., Pacucci, F., & Hickox, R. C. 2025, ApJ, 985, 169
Eisenstein, D. J., Johnson, B. D., Robertson, B., et al. 2023b, arXiv:2310.12340
Eisenstein, D. J., Willott, C., Alberts, S., et al. 2023a, arXiv:2306.02465
Ellison, S. L., Viswanathan, A., Patton, D. R., et al. 2019, MNRAS, 487, 2491
Endsley, R., Stark, D. P., Whitler, L., et al. 2023, MNRAS, 524, 2312
Endsley, R., Stark, D. P., Whitler, L., et al. 2024, MNRAS, 533, 1111
Feltre, A., Charlot, S., & Gutkin, J. 2016, MNRAS, 456, 3354
Ferland, G. J., Porter, R. L., van Hoof, P. A. M., et al. 2013, RMxAA, 49, 137
Ferruit, P., Jakobsen, P., Giardino, G., et al. 2022, A&A, 661, A81
Feuillet, L. M., Meléndez, M., Kraemer, S., et al. 2024, ApJ, 962, 104
Freeman, P. E., Izbicki, R., Lee, A. B., et al. 2013, MNRAS, 434, 282
Furtak, L. J., Labbé, I., Zitrin, A., et al. 2024, Natur, 628, 57
Furtak, L. J., Zitrin, A., Plat, A., et al. 2023, ApJ, 952, 142
Gabor, J. M., Capelo, P. R., Volonteri, M., et al. 2016, A&A, 592, A62
Gardner, J. P., Mather, J. C., Abbott, R., et al. 2023, PASP, 135, 068001
Gburek, T., Siana, B., Alavi, A., et al. 2019, ApJ, 887, 168
Giavalisco, M., Ferguson, H. C., Koekemoer, A. M., et al. 2004, ApJ, 600, L93
Greene, J. E., Labbe, I., Goulding, A. D., et al. 2024, ApJ, 964, 39
Greene, J. E., Seth, A., Kim, M., et al. 2016, ApJ, 826, L32
Greene, J. E., Strader, J., & Ho, L. C. 2020, ARA&A, 58, 257
Guo, Y., Ferguson, H. C., Bell, E. F., et al. 2015, ApJ, 800, 39
Gutkin, J., Charlot, S., & Bruzual, G. 2016, MNRAS, 462, 1757
Hainline, K. N., Johnson, B. D., Robertson, B., et al. 2024, ApJ, 964, 71
Hainline, K. N., Maiolino, R., Juodzbalis, I., et al. 2025, ApJ, 979, 138
Harikane, Y., Zhang, Y., Nakajima, K., et al. 2023, ApJ, 959, 39
Harris, C. R., Millman, K. J., van der Walt, S. J., et al. 2020, Natur, 585, 357
Hewlett, T., Villforth, C., Wild, V., et al. 2017, MNRAS, 470, 755
Iani, E., Rinaldi, P., Caputi, K. I., et al. 2025, ApJ, 989, 160
Illingworth, G. 2015, Hubble Legacy Fields ("HLF"), STScI/MAST, doi:10.17909/T91019
Izotov, Y. I., Thuan, T. X., & Guseva, N. G. 2007, ApJ, 671, 1297
Jakobsen, P., Ferruit, P., Alves de Oliveira, C., et al. 2022, A&A, 661, A80
Juodžbalis, I., Ji, X., Maiolino, R., et al. 2024a, MNRAS, 535, 853
Juodžbalis, I., Maiolino, R., Baker, W. M., et al. 2024b, Natur, 636, 594
Killi, M., Watson, D., Brammer, G., et al. 2024, A&A, 691, A52
Kocevski, D. D., Barro, G., McGrath, E. J., et al. 2023a, ApJ, 946, L14
Kocevski, D. D., Finkelstein, S. L., Barro, G., et al. 2025, ApJ, 986, 126
Kocevski, D. D., Onoue, M., Inayoshi, K., et al. 2023b, ApJ, 954, L4
Kokorev, V., Caputi, K. I., Greene, J. E., et al. 2024a, ApJ, 968, 38
Kokorev, V., Chisholm, J., Endsley, R., et al. 2024b, ApJ, 975, 178
Kokorev, V., Fujimoto, S., Labbe, I., et al. 2023, ApJ, 957, L7
Kokubo, M., & Harikane, Y. 2024, arXiv:2407.04777
Kroupa, P. 2001, MNRAS, 322, 231
Labbé, I., Greene, J. E., Bezanson, R., et al. 2023a, ApJ, 978, 92
Labbé, I., van Dokkum, P., Nelson, E., et al. 2023b, Natur, 616, 266
Larson, R. L., Finkelstein, S. L., Kocevski, D. D., et al. 2023, ApJ, 953, L29
Leja, J., Carnall, A. C., Johnson, B. D., Conroy, C., & Speagle, J. S. 2019, ApJ, 876, 3
Lin, X., Egami, E., Sun, F., et al. 2025, arXiv:2504.08028
Lotz, J. M., Primack, J., & Madau, P. 2004, AJ, 128, 163
Lyu, J., Alberts, S., Rieke, G. H., & Rujopakarn, W. 2022, ApJ, 941, 191
Lyu, J., Alberts, S., Rieke, G. H., et al. 2024, ApJ, 966, 229
Mager, V. A., Conselice, C. J., Seibert, M., et al. 2018, ApJ, 864, 123
Maiolino, R., Risaliti, G., Signorini, M., et al. 2025, MNRAS, 538, 1921
Maiolino, R., Scholtz, J., Curtis-Lake, E., et al. 2024a, A&A, 691, 145
Maiolino, R., Scholtz, J., Witstok, J., et al. 2024b, Natur, 627, 59
Matsuoka, Y., Onoue, M., Kashikawa, N., et al. 2019, ApJ, 872, L2
Matthee, J., Naidu, R. P., Brammer, G., et al. 2024, ApJ, 963, 129
Mazzolari, G., Übler, H., Maiolino, R., et al. 2024, A&A, 691, 345
Murray, S. G., Power, C., Robotham, A. S. G., et al. 2013, A&C, 3, 23
Nakajima, K., & Maiolino, R. 2022, MNRAS, 513, 5134
Nakajima, K., Ouchi, M., Isobe, Y., et al. 2023, ApJS, 269, 33
Navarro-Carrera, R., Caputi, K. I., Iani, E., et al. 2024, arXiv:2407.14201

Nevin, R., Blecha, L., Comerford, J., & Greene, J. 2019, ApJ, 872, 76
Oesch, P. A., Brammer, G., Naidu, R. P., et al. 2023, MNRAS, 525, 2864
Oesch, P. A., Brammer, G., van Dokkum, P. G., et al. 2016, ApJ, 819, 129
Oke, J. B., & Gunn, J. E. 1983, ApJ, 266, 713
Pacucci, F., Nguyen, B., Carniani, S., Maiolino, R., & Fan, X. 2023, ApJ, 957, L3
The pandas development team 2024, pandas-dev/pandas: Pandas, v2.2.3, doi:10.5281/zenodo.13819579
Parlanti, E., Carniani, S., Übler, H., et al. 2024, A&A, 684, A24
Pawlik, M. M., Wild, V., Walcher, C. J., et al. 2016, MNRAS, 456, 3032
Pérez-González, P. G., Barro, G., Annunziatella, M., et al. 2023a, ApJ, 946, L16
Pérez-González, P. G., Barro, G., Rieke, G. H., et al. 2024, ApJ, 968, 4
Pérez-González, P. G., Costantin, L., Langeroodi, D., et al. 2023b, ApJ, 951, L1
Peterson, B. M. 1997, An Introduction to Active Galactic Nuclei (Cambridge: Cambridge Univ. Press)
Peth, M. A., Lotz, J. M., & Freeman, P. E. 2016, MNRAS, 458, 963
Pierce, J. C. S., Tadhunter, C., Ramos Almeida, C., et al. 2023, MNRAS, 522, 1736
Reines, A. E., Greene, J. E., & Geha, M. 2013, ApJ, 775, 116
Richards, G. T., Lacy, M., Storrie-Lombardi, L. J., et al. 2006, ApJS, 166, 470
Rieke, M., Robertson, B., Tacchella, S., et al. 2023, Data from the JWST Advanced Deep Extragalactic Survey (JADES), STScI/MAST, doi:10.17909/8TDJ-8N28
Rieke, M. J., Kelly, D. M., Misselt, K., et al. 2023, PASP, 135, 028001
Rinaldi, P., Caputi, K. I., Costantin, L., et al. 2023, ApJ, 952, 143
Rinaldi, P., Caputi, K. I., Iani, E., et al. 2024, ApJ, 969, 12
Rinaldi, P., Pérez-González, P. G., Rieke, G. H., et al. 2025, arXiv:2504.01852
Rodriguez-Gomez, V., Snyder, G. F., Lotz, J. M., et al. 2019, MNRAS, 483, 4140

Rubinur, K., Das, M., Kharb, P., et al. 2024, MNRAS, 528, 4432
Rybicki, G. B., & Lightman, A. P. 1979, Radiative processes in astrophysics (New York: Wiley)
Sanders, R. L., Shapley, A. E., Kriek, M., et al. 2016, ApJ, 816, 23
Scholtz, J., Maiolino, R., D'Eugenio, F., et al. 2025, A&A, 697, A175
Setton, D. J., Greene, J. E., de Graaff, A., et al. 2024, arXiv:2411.03424
Shah, E. A., Kartaltepe, J. S., Magagnoli, C. T., et al. 2020, ApJ, 904, 107
Sheth, R. K., Diaferio, A., Hui, L., & Scoccimarro, R. 2001, MNRAS, 326, 463
Tacchella, S., Eisenstein, D. J., Hainline, K., et al. 2023, ApJ, 952, 74
Taylor, M. 2022, in ASP Conf. Ser. 532, Astronomical Data Analysis Software and Systems XXX, ed. J. E. Ruiz, F. Pierfederici, & P. Teuben (San Francisco, CA: ASP), 3
Treu, T., Calabrò, A., Castellano, M., et al. 2023, ApJ, 942, L28
Tripodi, R., D'Eugenio, F., Maiolino, R., et al. 2024, A&A, 692, A184
Trouille, L., Barger, A., & Tremonti, C. 2011, AAS Meeting, 217, 326.03
Trump, J. R., Arrabal Haro, P., Simons, R. C., et al. 2023, ApJ, 945, 35
Übler, H., Maiolino, R., Curtis-Lake, E., et al. 2023, A&A, 677, A145
Übler, H., Maiolino, R., Pérez-González, P. G., et al. 2024, MNRAS, 531, 355
Villforth, C., Hamann, F., Rosario, D. J., et al. 2014, MNRAS, 439, 3342
Wang, B., de Graaff, A., Davies, R. L., et al. 2025, ApJ, 984, 121
Whitaker, K. E., Ashas, M., Illingworth, G., et al. 2019, ApJS, 244, 16
Williams, C. C., Alberts, S., Ji, Z., et al. 2024, ApJ, 968, 34
Williams, C. C., Tacchella, S., Maseda, M. V., et al. 2023, ApJS, 268, 64
Wright, G. S., Rieke, G. H., Glasse, A., et al. 2023, PASP, 135, 048003
Wu, K. L.-K. 1999, PhD thesis, Univ. of California
York, D. G., Adelman, J., Anderson, J. E., Jr., et al. 2000, AJ, 120, 1579
Yue, M., Eilers, A.-C., Ananna, T. T., et al. 2024, ApJL, 974, L26
Zeimann, G. R., Ciardullo, R., Gebhardt, H., et al. 2015, ApJ, 798, 29
Zhang, J., Egami, E., Sun, F., et al. 2025, arXiv:2505.02895